

Mechanofusion-derived cathode composite microstructures with scalable mixed conducting matrix coatings for solid state batteries

Received: 4 June 2025

Accepted: 4 March 2026

Cite this article as: Kissel, M., Frankenberg, F., Demuth, T. *et al.* Mechanofusion-derived cathode composite microstructures with scalable mixed conducting matrix coatings for solid state batteries. *Nat Commun* (2026). <https://doi.org/10.1038/s41467-026-71305-2>

Maximilian Kissel, Finn Frankenberg, Thomas Demuth, Anton Lai, Niklas Laser, Daniel Wagner, Ahmed Eisa, Peter Michalowski, Kerstin Volz, Arno Kwade & Jürgen Janek

We are providing an unedited version of this manuscript to give early access to its findings. Before final publication, the manuscript will undergo further editing. Please note there may be errors present which affect the content, and all legal disclaimers apply.

If this paper is publishing under a Transparent Peer Review model then Peer Review reports will publish with the final article.

Mechanofusion-derived cathode composite microstructures with scalable mixed conducting matrix coatings for solid state batteries

Maximilian Kissel^{1,†}, Finn Frankenberg^{2,†}, Thomas Demuth³, Anton Lai¹, Niklas Laser², Daniel Wagner¹, Ahmed Eisa², Peter Michalowski², Kerstin Volz³, Arno Kwade^{2,}, Jürgen Janek^{1,*}*

¹Justus-Liebig-Universität Gießen, Institute of Physical Chemistry & Center for Materials Research, Heinrich-Buff-Ring 17, Gießen, 35392, Hesse, Germany

²Technische Universität Braunschweig, Institute for Particle Technology, Volkmaroder Straße 5, Braunschweig, 38104, Lower Saxony, Germany

³Materials Science Center (WZMW) and Department of Physics, Philipps-University Marburg, Marburg 35032, Hesse, Germany

*Corresponding authors:

E-mail: juergen.janek@pc.jlug.de; arno.kwade@tu-braunschweig.de

† These authors contributed equally to this work

Abstract

The successful implementation of solid state batteries not only requires the use of high-capacity anodes, but also high-performance composite cathodes. However, the production of solid state battery cathode composites with optimized microstructures remains a significant challenge, especially for large-scale fabrication. Here, we present a scalable high-intensity dry mixing process to create tailored functional coatings on single-crystalline $\text{LiNi}_{0.82}\text{Mn}_{0.07}\text{Co}_{0.11}\text{O}_2$ via mechanofusion. We investigate the coating of $\text{LiNi}_{0.82}\text{Mn}_{0.07}\text{Co}_{0.11}\text{O}_2$ with the malleable halide solid electrolyte Li_3InCl_6 under various process conditions, linking process parameters obtained from discrete element method simulations with experimentally accessible morphological properties to offer guidelines for further optimization. In this way nanometer-thin covering coatings as well as thick matrix coatings are successfully produced. Incorporating carbon black into the thick matrix coating results in well-performing mixed conducting matrices that can be used directly as composite cathodes without further treatment. The compositions investigated enable stable cycling with a specific capacity of up to $q_{\text{comp}} = 100 \text{ mAh g}^{-1}$ (based on the total mass of the composite cathode) at a C-rate of 1C (60 min). While higher carbon black content is observed to improve CAM utilization, excessive amounts are detrimental for cell kinetics and chemo-mechanics, emphasizing the importance of the cathode mixing process and composition on overall cell performance.

1. Introduction

Solid state batteries (SSBs) have emerged as a promising next-generation energy storage technology, aiming to overcome the safety and energy density limitations of conventional lithium-ion batteries (LIBs) that rely on liquid electrolytes (LEs).^{1,2} Replacing the LE with a solid electrolyte (SE) is expected to enable the implementation of high-energy anode (negative electrode) concepts such as lithium metal anodes³, ‘anode-free’ configurations⁴, or Si-based anodes⁵. To match these expected high performance anodes, equally high-performing cathodes (positive electrode) are required.^{6–8}

SSB cathodes are usually designed as composites of SE, cathode active material (CAM) and additive particles. Towards large-scale commercialization of SSBs, various challenges persist, starting at the material level.⁹ Here, research focuses on the one hand on developing advanced solid electrolytes with enhanced ionic conductivities^{10,11}, broader electrochemical stability windows^{12,13}, or beneficial mechanical properties¹⁴ and on the other hand scaling and sustainable SE production processes^{15,16}. Moreover, to mitigate degradation effects at the CAM|SE interface, the use of protective CAM coatings is required.^{17,18} As CAM, Ni-rich layered oxides^{19–21} are widely used with preference for materials that show beneficial chemo-mechanical properties, *i.e.*, low volume expansion^{22–24} and low tendency for cracking^{25,26} – as seen in single crystals, which showed improved long-term cycling performance.^{9,27–30}

Not only the materials in the cathode but especially their arrangement, *i.e.*, the composite microstructure, is crucial for the performance.^{7,31–33} The microstructure needs to fulfil three main tasks: First, the CAM particles need to be electronically and ionically connected, *i.e.*, electrochemically active, leading to a high CAM utilization within a percolating network. As recently highlighted by Kissel *et al.*³⁴, achieving a complete static CAM utilization is not self-evident in SSBs. Second, the electronic and ionic network should possess high effective

conductivities for an improved kinetic cell performance.^{35–38} Lastly, intimate and mechanically as well as (electro)chemically stable solid-solid contacts between the CAM and the SE are crucial to enable fast charge transfer at the interface, while also accommodating the volume expansion of the CAM during charging and discharging.^{39,40}

The final SSB cathode microstructure is largely defined during the particle mixing process, since in contrast to LIBs, SSBs do not allow infiltration of the cathode with an electrolyte post-assembly. However, despite its importance and challenges toward large-scale implementation^{41–43}, the actual mixing process has received relatively little attention up to now.^{44–47} In academic studies hand mortaring is common although this is non-scalable and suffers from reproducibility issues.^{34,48} On the other hand, machine-made composites are becoming more prevalent in recent studies^{34,43,49,50}. Further processing-related approaches have focused on comminuting SE particles before mixing to achieve a tailored particle size distribution (PSD).^{49,51–54} While this is crucial to match the CAM PSD^{7,38,52} it involves additional processing steps that can damage the SEs by solvents⁵⁵ or by the milling itself^{49,56}. Other approaches are based on solution processes to apply SE coatings on active materials or to infiltrate porous electrodes.^{57,58} In general, only few studies explore scalable composite mixing machines for SSB cathode composites and in most cases the corresponding mixing process leads to a more or less “random” ordering of particles.^{7,43,47}

Recently, employing a combined modelling and experimental approach, W. Lee *et al.*⁵⁹ introduced the concept of building blocks towards an ideal cathode composite microstructure. Building blocks describe the fundamental units of a composite’s microstructure in the form of tailored particle aggregates. By engineering these building blocks, the overall microstructure and thus the resulting material properties can be precisely controlled. D. Lee *et al.*⁴⁰ highlighted the importance of shear forces which increase the electrolyte-covered surface area of the active materials. Kawaguchi *et al.*^{60,61} and Hayakawa *et al.*^{62,63} investigated the idea of coating low- and

medium-nickel $\text{Li}_x\text{Ni}_y\text{Co}_z\text{Mn}_{1-y-z}\text{O}_2$ (NCM) particles with SE in a high-intensity mixer. Kim *et al.*³⁹ utilized mechanofusion as a preprocessing step to ensure intimate interfacial contact by coating NCM with $\text{Li}_6\text{PS}_5\text{Cl}$ (LPSCl). This allowed a high CAM loading in the cathode and led to higher specific capacities. However, sole coating with SE is not sufficient since it impedes electron transfer which would only be possible via CAM-CAM particle contacts after deforming parts of the SE coating layer during densification. To overcome this limitation, the authors added carbon additives to their SE-coated CAM and had to manually mortar the composite once again.³⁹

Inspired by these recent works, we systematically investigate a dry particle coating approach, based on mechanofusion, in this study to create tailored building blocks for SSB composite cathode microstructures. Going beyond the idea of simple mixing of loose particles and arbitrary (re-)ordering, we employ a scalable high-intensity mixing process to create a defined mixed conducting matrix coating via mechanofusion on single crystalline Ni-rich $\text{LiNi}_{0.82}\text{Mn}_{0.07}\text{Co}_{0.11}\text{O}_2$ (NCM82) without any hand mortaring being involved. In this bottom-up approach, which can also be used to produce protective CAM coatings, we make use of the good deformability of the halide SE Li_3InCl_6 (LIC) as model catholyte. We investigate the effect of composition and process parameters on the morphology of the coating, coating progress and possible degradation of the materials, combining scanning electron microscopy (SEM), energy-dispersive X-ray spectroscopy (EDX), (scanning) transmission electron microscopy ((S)TEM) and X-ray photoelectron spectroscopy (XPS). We link experimental results with stressing conditions obtained from discrete element method (DEM) process simulations to describe the coating process on the macroscale. In this way, we establish a basis for future optimization of the mixing process of composite cathodes. We demonstrate that the presented mechanofusion process is suitable to produce thin covering coatings as well as thick matrix coatings. By adding carbon black (CB) into the matrix, the coatings become mixed conducting and are further electrochemically analyzed in

detail. Our results show that the mixed conducting matrix coating design approach via mechanofusion is promising as a versatile and scalable production method for SSB composite, while still offering significant potential for further optimization.

ARTICLE IN PRESS

2. Results

Fig. 1 illustrates the concept of the mixed conducting matrix coating approach employed in this study. Cathode composites, comprising three components with different PSDs, were fabricated using single crystalline NCM82, in the following denoted as NCM, with a median particle size of $d_{50} = 3.3 \mu\text{m}$ as CAM, in-house prepared LIC (see Methods) with particle sizes ranging from 100 nm to 100 μm as SE and carbon black (CB, $d_{50,\text{aggregates}} \approx 250 \text{ nm}$) as electron conducting additive (Fig. 1a).

The particles were mixed in a scalable and commercially available high-intensity mixer (Fig. 1b) which provides high shear forces within the narrow gap⁴³ enabling mechanofusion.^{39,45,64,65} During this process, the NCM particles act as host particles that are coated with guest particles (here: LIC or premix of LIC & CB, see Table 1 and Methods) forming core-shell type heteroaggregates as depicted in Fig. 1c. These aggregates are hereafter referred to as building blocks, following the concept introduced by Lee *et al.*⁵⁹ and are denoted by their composition as NCM:LIC:CB (w/w/w). Process parameters that can be varied during the high-intensity mixing are the rotational speed n , the mixing time t_{mix} and the filling degree φ . By adjusting these parameters, the properties of the building blocks in this bottom-up approach, and thus the overall microstructure of the cathode composite (Fig. 1d), can be significantly influenced. Towards scalable cathode composite production, all mixtures in this work were prepared in a dry room with a dew point of the supply air of $-60 \text{ }^\circ\text{C}$ without any manual hand mortaring being involved. All mixtures were prepared with a batch size of approximately 20 g, corresponding to a filling degree of 10%. In total, three main investigations (cf. Table 1 and Table S1) were conducted and are discussed in the following.

First, the coating thickness of the building blocks was varied by systematically adjusting the ratio of SE (and CB) to NCM, while maintaining constant process time and rotational speed.

Secondly, the influence of stress intensity or shear stress, as well as collision number respectively, during mixing was investigated by varying the rotational speed and mixing time for two specific compositions. Third, the mixed conducting matrix coating with a weight ratio of 80:20: x (NCM:LIC:CB) was optimized by altering the CB content x , aiming at achieving a balance between electronic and ionic partial conductivity within the building blocks.

2.1. Impact of composition on coating morphology

To investigate the effect of coating material content on the morphology and homogeneity of the coating, different mixtures with coating contents ranging from 1 to 20 wt.% were processed at a rotational speed of 10,000 rpm, corresponding to a tip speed of 40 m s^{-1} , for 60 minutes. As guest particles during the mechanofusion process, pure LIC as well as a LIC-CB mixture with a fixed CB:LIC ratio of 20 vol.% CB was used (cf. Table S1). Scanning electron microscopy (SEM) combined with energy-dispersive X-ray spectroscopy (EDX) was carried out to visualize the morphology of the coating within the building blocks.

Fig. 2a shows that a coating is achieved for all cases independent of the coating material content. For all EDX acquisitions, the same parameters were used, so that differences in signal intensity can be related to differences in the composition. As expected, the intensity of the chlorine signal, stemming from the coating, decreases with decreasing coating amount. The effect of the coating is further evidenced by the rounding of NCM particle edges, reflected in a decreased aspect ratio and an increased circularity with rising coating material content (Supplementary Figure S1). This indicates that the coating material fills recessed regions of the NCM particles, leading to a varying thickness across the particle surface (Supplementary Figure S1e). Intergranular boundaries existing within aggregates of the bare NCM disappear completely for high coating amounts showing that the coating material is covering these areas (Supplementary Figure S2). Especially at high coating material contents, an increase in volume-based particle size Q_3 is observed, which

is based on the increase in coating thickness (Fig. 2b). However, the coating as such is not the determining factor for this increase, since a theoretical maximum average coating thickness of approximately 150 nm is expected (Supplementary Figure S3). Rather, multiple agglomerated NCM particles are surrounded by a coating layer, which means that one particle is visible under the SEM and counted in the PSD calculation, but in fact several NCM particles are encapsulated by the coating. Since encapsulation occurs only for some agglomerated NCM clusters, a pronounced broadening of the particle size distribution is observed with increasing coating content. From the broadening of the PSD in combination with the increasing amount of soft coating with increasing coating material content, it can be supposed that the interparticle spaces can be better filled and thus the building blocks can be better packed in the final cathode composite microstructure. This improved packing is indeed reflected in the measured bulk porosity of the cathode composites which decreases with increasing coating content (Fig. 2c). The porosity of the composite mixtures containing CB is consistently slightly lower than that of the composites without CB. We attribute this to the higher volume fraction of compressible components in the formulations containing CB, which increases from 31.4 % to 35.6 % for the 80:20 and 80:20:3 compositions, respectively. For the highest coating amount, the porosity measured at a compaction pressure of 3.45 MPa was about 25 %. This value corresponds approximately to the porosity of a cubic closed packing of spheres. For a higher compaction pressure, we expect more deformation of the coatings and thus a reduced porosity of the composite cathode.

Transmission electron microscopy (TEM) images confirm a homogenous coating layer, exemplarily depicted for a high and low coating amount in Fig. 3. In dark-field imaging of a composition of 80:20:1, some crystals in the coating layer appear bright (Fig. 3a). These bright regions are lattice planes of small crystals (cf. Supplementary Figure S4a) with random orientations towards the position of the objective lens aperture. X-ray diffractograms

(Supplementary Figure S5) confirm that crystalline phase of the LIC is preserved and the mass ratios after Rietveld refinement (Supplementary Table S3) are in line with the expected values, indicating that there is no significant amorphization happening. Corresponding Scanning STEM-EDX maps (Fig. 3b and Supplementary Figure S4b) reveal the presence of carbon in the approximately 100 nm thick coating layer, indicating that the desired mixed conducting matrix coating was achieved. In case of the 99:1:0 composition, the coating is only approximately 5 nm thick (Fig. 3c,d) and consistently observed along the entire particle surface (Supplementary Figure S6). Variations in signal intensity across the EDX maps in Fig. 3b,d are attributed to differences in particle orientation relative to the detector, which can influence the intensity of the detected signal.

To further quantify the homogeneity and thickness of the coating, X-ray photoelectron spectroscopy (XPS) was carried out. Based on the signal intensities of the NCM and coating elements, values for the coverage γ of the building blocks were calculated which represent the signal intensity ratio of coating to NCM (see Methods and reference ⁶⁶ for details). The coverage value describes how strongly the signal of the NCM particle is shielded by the coating. It depends on the thickness, the composition (with or without CB), the morphology and the homogeneity of the coating. A coverage value close to 1 indicates nearly complete surface coverage and the presence of a relatively thick coating layer (cf. Fig. 4a), such that almost no signals from the NCM are detected. This situation corresponds to coating thicknesses of at least ~10 nm, which is approximately the information depth of XPS measurements. While the coverage value itself does not provide information on the morphology or local thickness distribution, it enables assessing whether a continuous coating layer is formed across a broad range of process parameters. For coatings expected to be thinner than ~10 nm (cf. Supplementary Figure S3), the coverage value derived from XPS no longer reflects the true surface coverage. In this case, even a perfectly

covering coating layer will never result in a coverage value of 1, since signals stemming from the NCM can always be detected. Conversely, coatings that are uniformly thicker than at least ~10 nm cannot be distinguished from one another by this method, as all yield coverage values close to 1. As displayed in Fig. 4b, the coverage increases with increasing coating content, which we attribute to the rise in coating thickness. It is also evident that the incorporation of CB in the coating, especially at low coating thicknesses, leads to larger coverage values. Since the weight ratios are kept constant, the coatings that also contain CB occupy a larger volume due to low (bulk) density of CB. Thus, the signals of the NCM are more strongly shielded, yielding higher coverage values than the CB-free counterparts. At a high coating content corresponding to the ratio 80:20:3, the maximum possible coverage value of 1 is reached which indicates that the NCM particles are fully covered. This confirms the previously discussed SEM and STEM measurements.

The results demonstrate that high intensity mixing leading to mechanofusion is a well-suited method for the dry production of core-shell structures with various coating thicknesses. This is particularly attractive for protective coatings employing soft SEs, a promising concept that has recently gained attraction to prevent interfacial degradation in SSB cathode composites.^{65–67}

2.2. Investigation of Process-Structure-Relations

In the following, we focus on the 80:20:3 composition, which is designed to serve as a matrix coating since it reaches the highest degree of coverage. To investigate the coating progress as function of process conditions, the composition was produced at different speeds and mixing times.

During high-intensity mixing, mechanical energy is transferred to the particle system through the high relative velocities generated between the rapidly rotating rotor and the surrounding particles. This energy transfer is reflected in the specific energy input $E_{m,exp}$ which is significantly influenced by the rotational speed and mixing time. This was estimated

experimentally for the different coating experiments from the measured power P , idle power P_0 , sample mass m_{total} , and mixing time t_{mix} (cf. Supplementary Figure S7).

$$E_{\text{m,exp}} = \frac{\int (P - P_0) dt}{m_{\text{total}}} \quad 1$$

To evaluate the coating progression, the coverage of the 80:20:3 composition is depicted in Fig. 5a as a function of the specific energy input. At lower rotational speeds of 1,000 rpm and 2,500 rpm, coverage increases with prolonged mixing time and thus specific energy input. In contrast, at higher rotational speeds of $n \geq 5,000$ rpm, a maximum coverage of 97% – 100 % (dashed grey region) is reached within just 5 minutes to 10 minutes of mixing. Extending the mixing time up to 60 minutes, results in only marginal changes in coverage values at these higher rotational speeds. A similar trend is observed for a composition of 95:5:0.8 (cf. Supplementary Figure S8a).

As discussed, similar coverage levels do not necessarily indicate comparable coating morphologies (cf. Fig. 4a). Porosity measurements show a consistent decline in porosity of the cathode composites with increasing specific energy input (Fig. 5b). The reduction in porosity indicates that even when coverage values reach a plateau, the morphology of the building blocks can continue to evolve significantly with varying processing conditions. This is corroborated by SEM images as seen in Fig. 5c for the samples processed at different rotational speeds (see also Supplementary Figure S9). At 1,000 rpm, only an inhomogeneous and particulate deposition of CB and LIC on the NCM particles can be seen, forming cluster-like agglomerates. Moreover, single LIC particles are visible which have not taken part in the coating process. At 5,000 rpm, individual LIC and CB particles remain discernible on the NCM surface, whereas at 10,000 rpm, the NCM particles are uniformly encapsulated by a smooth coating layer. According to

mechanofusion theory⁶⁸ different coating structures can form at different rotational speeds, ranging from loosely adhered particles to continuous shells. In our case, continuous and smooth shells are observed at high rotational speeds and long mixing times, while lower speeds and reduced energy input tend to result in coatings consisting of loosely adhered particles.

Overall, the coating morphology becomes smoother and less particulate with increasing specific energy input and, at comparable specific energy input, with increasing rotational speed and thus mixer intensity. This leads to an increase in the circularity of the building blocks, as shown for the rotational speeds of 1,000 rpm, 5,000 rpm and 10,000 rpm mixed for 60 minutes. Coverage metrics derived from XPS analyses cannot fully resolve these morphological features which requires complementary SEM analysis.

2.3. Linking DEM simulations and experiments

To enable a guided optimization of the mechanofusion process for production of SSB cathode composites, we carried out DEM simulations to simulate the stresses acting on the particles in the high-intensity mixer. As elaborated in the Methods section and Supplementary Note 3, a coarse-graining approach was applied to handle the extremely high number of real particles. While this approach does not retain information on the original coating progression, it allows for the determination of the mixer's overall stressing conditions. Calibration tests have been carried out to determine apparent properties of the coarse-grained particles to mimic the original situation. To validate the calibration procedure and calculated coarse-grain density of the coarse-grained particles (Fig. 6b & Supplementary Figure S10 and Table S2), the mean specific power obtained from the experiments was first compared with the specific power obtained from the DEM simulation in the steady state. Both specific power data show a high degree of agreement, confirming the successful calibration of the particle properties.

In order to quantitatively describe the process and compare process parameters, we applied the stressing model of Kwade⁶⁹, which uses the stress energy or stress intensity, respectively, and stress frequency or stress number, respectively, as parameters to calculate the specific energy input E_m based on these model parameters. This allows a quantitative comparison of various process conditions.^{70,71} According to **Equation 2**, $E_{m,sim}$ is expressed as product of the mean stress intensity \overline{SI}_{CG} of the particle collisions, corresponding to the mean dissipated energy during coarse-grained particle collisions related to stressed coarse-grain mass and the mean stress number per particle \overline{SN}_p . The \overline{SN}_p can be determined by the frequency of collisions of the coarse-grain particles during mixing SF_{CG} divided by the number of coarse-grains, which is obtained from the ratio of the individual particle mass $m_{particle,CG}$ to total mass m_{total} , and the mixing time t_{mix} . Both parameters \overline{SI}_{CG} and \overline{SN}_p should be approximately scale-invariant (Supplementary Note 3) and are obtained from DEM simulations^{43,72} to calculate the simulation-based $E_{m,sim}$.

$$E_{m,sim} = \frac{\overline{SI}_{CG} \cdot m_{particle,CG} \cdot SF_{CG} \cdot t_{mix}}{m_{total}} = \overline{SI}_{CG} \cdot \overline{SN}_p \quad 2$$

In the following, the parameters \overline{SI}_{CG} and \overline{SN}_p are used to describe the mechanofusion process macroscopically. Both are individually influenced by the rotational speed n and t_{mix} , thus affecting the progression and morphology of the coating. \overline{SI}_{CG} is highest near the rotor tip and in the gap between the rotor tip and the mixer wall (Fig. 6a), primarily governed by the rotational speed of the mixer for a constant gap width. An approximate increase of $\overline{SI}_{CG} \propto n^2$ can be expected with increased rotational speed⁴³, potentially influencing the building block microstructure. In contrast, \overline{SN}_p depends on both the rotational speed and t_{mix} . Therefore, an

equivalent energy input can be achieved at lower \overline{SI}_{CG} if compensated by a higher \overline{SN}_p through extended mixing times, although this may result in a different coating morphology.

To understand the individual influence of \overline{SI}_{CG} and \overline{SN}_p , stress frequency – stress intensity curves were generated from the recorded particle collisions and served as the basis for determining \overline{SN}_p and \overline{SI}_{CG} . The coverage of the 80:20:3 mixtures was plotted against both parameters (Fig. 6c,d). Fig. 6c shows that an increasing \overline{SI}_{CG} generally leads to higher coverage values. Notably, at a \overline{SI}_{CG} corresponding to 5,000 rpm ($\overline{SI}_{CG} = 0.123 \text{ J kg}^{-1}$), nearly complete coverage ($> 97 \%$) is achieved after only 5 minutes of mixing. Further increasing \overline{SI} beyond this point results in only slight changes in coverage. However, significant changes in coating morphology that occur at constant mixing time, but varying stress intensities as already shown in Fig. 5a (see also Supplementary Figure S9) become visible.

When the coverage is analyzed as a function of \overline{SN}_p (Fig. 6d), it becomes clear that there is no direct proportionality. An equivalent or even higher \overline{SN}_p (region 1) does not achieve the same degree of coverage but depends on the \overline{SI}_{CG} . This indicates that elevated \overline{SI}_{CG} (region 2), associated with higher collision energies, are beneficial for forming a uniform coating with higher coverages. Nevertheless, even at lower \overline{SI}_{CG} such as 0.006 J kg^{-1} (1,000 rpm) and 0.033 J kg^{-1} (2,500 rpm), the coverage gradually increases with \overline{SN}_p due to extended mixing times. However, to achieve more than 97 % coverage with a \overline{SI}_{CG} equivalent to 2,500 rpm and 1,000 rpm, longer mixing times would be required. Even then, the resulting coating morphology is likely to differ significantly, as already observed at higher rotational speeds (5,000 rpm and 10,000 rpm), where 97% coverage was also achieved (cf. Fig. 5c). From a process engineering and economic perspective, long mixing times are impractical. Therefore, a higher \overline{SI}_{CG} is preferable to ensure efficient coating formation within reasonable processing times.

To achieve both high coverage and improved homogeneity, the highest \overline{SI} investigated (10,000 rpm) appears to be the most effective choice for the given material system and composition. However, at these high collision energies, potential degradation effects should be monitored including for instance structural damage and strain in the NCM particles as well as elemental interdiffusion at the NCM|coating interface. Structural integrity was probed via scanning precession electron diffraction (SPED) in the TEM. In the darkfield TEM shown in Fig. 7a, the NCM particles appear dark, whereas the coating layer is brighter with distinct bright spots. In the region marked with a red box, a SPED phase map was recorded (Fig. 7b). Thereby, only the pristine layered phase and the coating layer were detected with no evidence of a rock salt-type phase in the NCM surface region, that would be indicative of NCM degradation. This observation was further confirmed by manually inspecting the diffraction patterns at the interface, which did not show any signs of degradation. Additional XRD measurements and Rietveld refinement likewise revealed no significant changes in lattice parameters or strain (Supplementary Figure S12 and Table S3). The chemical stability at the interface was probed using STEM-EDX (Supplementary Figure S13). The element map (Supplementary Figure S13a) shows the CB-LIC matrix around the NCM particles. To check for elemental interdiffusion, a line scan across the interface was evaluated (Supplementary Figure S13b). Due to the NCM surface being slightly slanted, the characteristic compositions of NCM and LIC overlap in a small interfacial region (Supplementary Figure S13c). However, no evidence of elemental diffusion beyond this overlapping region of approximately 10-15 nm width was detected. Based on these observations, we assume that the coating process in the high-intensity mixer does not damage the NCM surface region. Rather, the small single-crystalline particles appear to tolerate the processing conditions. In addition, the softer LIC phase is expected to exert a dampening effect.

It is important to note, however, that this may differ when processing other material systems, such as larger polycrystalline CAM particles or sulfide SEs.⁷³ Larger particles exhibit typically a higher defect probability, due to a lower particle strength than for aggregates, according to Rumpf⁷⁴, scales as $\sigma \propto \frac{1}{d^2}$, and for primary particles, according to Tavares and King⁷⁵ scales as $\sigma \propto \frac{1}{d^{1.2}}$, making fragmentation more likely at similar stress intensities. To corroborate this, we conducted a mixing experiment with larger polycrystalline NCM particles under the same high stressing conditions applied in this study (10,000 rpm for 60 min). The results show that, although most particles retained their overall structure, few fragmented particles were observed (Supplementary Figure S14). Notably, these were consistently among the largest particles, which supports both our considerations. Moreover, applying a mill (e.g. planetary ball mill) for the composite mixing can result in higher stress intensities and might also cause material degradation of the single crystal NCM^{71,76}.

In these cases, DEM simulations could provide guidance for process optimization, indicating that lower stress intensities, which might be necessary to prevent chemical or structural degradation during processing, can be compensated by longer mixing times to achieve similar coverages. For example, in the case of coating at 1,000 rpm, achieving a target coverage of approximately 97.5 % would require extending the mixing time by 200 %, *i.e.*, to a total of ~3 h. When combined with further degradation studies, DEM simulations can help identify suitable process parameters for different material systems and mechanofusion processes.

2.4. Electrochemical Performance of Mixed Conducting Matrix Coatings

Based on the investigations discussed above, a maximum stress intensity and maximum stress number, *i.e.*, a rotational speed of 10,000 rpm and a mixing time of 60 minutes, were selected as fixed process parameters to further study systematically the effect of carbon content in the matrix

on the electrochemical performance of the resulting matrix coating. In the following, we refer to the CB-LIC premix as the matrix, and to the NCM-LIC-CB mixture, *i.e.*, the coated NCM particles, as the composite.

Effective charge transport requires fast electronic and ionic pathways between the CAM particles and the current collectors. A matrix coating solely composed of low electron-conducting SE, *i.e.*, a composition of 80:20:0, is expected to limit the electronic transport. In this case, electrons can only be conducted via NCM-NCM point contacts after deformation of the SE coating layer. Thus, the idea is to add an electron conductive additive to form a mixed conducting matrix. A similar mixture, composed of CB and LPSCl, was already investigated by Reisacher *et al.*⁷⁷ to identify the necessary content of CB to achieve an electronically percolating matrix. Similarly, we evaluated different CB-LIC ratios to identify the percolation threshold p_c for our system.

To this end, we determined the partial electronic conductivities using direct current (DC) polarization in symmetric ion-blocking cells, both for the CB-LIC matrix as well as for the NCM-LIC-CB (80:20: x) composites with different compositions. As shown in Fig. 8a, the threshold for electronic percolation, p_c , in the matrix lies between 2 and 5 wt.%. Below this range, the partial electronic conductivity of the matrix remains below 0.01 mS cm^{-1} , while at 5 wt.%, it increases by four orders of magnitude to almost 200 mS/cm and further rises up to 1000 mS cm^{-1} at 15 wt.% CB. The cathode composites exhibit a similar trend for the electronic partial conductivity, which increases from approximately 0.03 mS cm^{-1} at 0 % CB to 1.8 mS cm^{-1} at 15 % CB in the matrix.

Since the mixed conducting matrix not only needs to provide electronic but also sufficient ionic conduction, we further measured the ionic partial conductivities of the different matrices and composites, respectively. Using DC polarization in symmetric electron-blocking cells, an opposite trend for the ionic conductivity as function of the CB content is observed (Fig. 8a). With increasing CB content, the ionic conductivity of the matrix decreases from about 0.7 mS cm^{-1} to 0.03 mS cm^{-1}

¹. Similarly, for the composites the ionic partial conductivity decreases as well. For the highest CB content, the minimum ionic partial conductivity of about 0.006 mS cm^{-1} was measured for the respective composite. The highest ionic partial conductivity of about 0.04 mS cm^{-1} was found for the composite with a CB content in the matrix of 1 wt.%.

The differences between maximum and minimum ionic conductivity values are not as large as for the electronic conductivity. Furthermore, not all datapoints follow a strict monotonic trend with increasing CB content. We attribute this observation to the fact that the CB is not equally homogeneously distributed in all samples leading to different microstructures. In general, the differences in conductivities deviating from the trend are rather small given the general level of uncertainty. Moreover, not only the materials are error-prone, but also the experimental conditions in the dry room might lead to irregularities.

At this point, we would like to highlight that the percolation behavior is not only dependent on the intrinsic material properties but also on the sample size of the considered volume used to determine the percolation threshold. During the measurement of the matrix, bulk properties are assessed, as a relatively large amount of powder is used to produce a thick pellet (Fig. 8b). The values obtained from these bulk-scale measurements are not necessarily representative of the situation when the matrix is applied as a thin coating. In this case, the coating is typically in the nanometer range, representing a finite-size system in which the percolation threshold p_c can be reached earlier, *i.e.*, at lower carbon black (CB) contents. Thus, the macroscopic bulk p_c derived from symmetrical cell setups should rather be viewed as an upper limit for the CB content in the composite.

Additionally, partial conductivities primarily describe charge transport through the bulk composite and offer no insights into the charge transfer kinetics at the cathode active material/solid electrolyte (CAM/SE) interface, particularly since the CAM is typically fully lithiated during such

measurements.³⁵ Therefore, the partial conductivities obtained from symmetrical cells do not necessarily correlate fully with the half-cell performance as recently also observed by Puls et al.

78.

This assumption is indeed reflected in the cycling performance of the half-cells depicted in Fig. 9a. Here, the cells with CB contents above the determined p_c (80:20:1/2/3) show a significantly worse performance than cells with CB contents below p_c . While the attainable capacities at 0.1C are still comparable, they rapidly decrease at 0.3C and 1C. For example, while providing an initial composite-specific capacity of $\sim 130 \text{ mAh g}^{-1}$ at 0.1C, the 80:20:3 composition can only supply a discharge capacity of less than 10 mAh g^{-1} at 1C. Interestingly, the composite without any CB in the matrix, *i.e.*, with a negligible electronic conductivity, exhibits a decent performance retaining approximately 85 mAh g^{-1} at 1C when being charged in constant current constant voltage (CCCV) mode. The electronic transfer across NCM-NCM point contacts seems to be sufficient at the tested stack pressure of about 80 MPa, confirming the previous results of Kim *et al.*³⁹. In the here presented work, we could achieve further improvement in cycling performance when adding some CB into the matrix. Among the tested compositions, the 80:20:0.5 composite delivers the highest composite specific discharge capacity of $q_{\text{comp}} = 100 \text{ mAh g}^{-1}$ at 1C after charging in CCCV mode. In the following, the cycling behavior depending on the cathode compositions shall be discussed in more detail.

All capacity values in Fig. 9a refer to the total mass of the composite, since this metric is closer to practically relevant performance indicators than CAM-specific capacities, which are shown together with the Coulombic efficiencies in Supplementary Figure S15 (see also Supplementary Note 4). As discussed in our previous work³⁴, not all CAM particles are necessarily electrochemically active in SSB composite cathodes. Depending on the cathode

composition and/or the mixing method, a substantial fraction of CAM can remain electronically disconnected and thus inactive, thereby lowering the overall static CAM utilization. Consequently, capacity values based on either the total mass of CAM or the total cathode mass reflect not the intrinsic active material properties but are strongly convoluted with the microstructure of the composite. Thereby, it is possible to differentiate between static and kinetic capacity losses.³⁴ Static capacity losses consider the issue of incomplete static CAM utilization which is non-negligible for the tested compositions as depicted in Fig. 9b. The highest CAM utilization of about 90 % is reached for the highest CB content, while in the low CB (0 to 0.5 %) containing composites only about 65 % of the CAM particles are electronically connected. This is reasonable since CB in the matrix is expected to facilitate the formation of electronic connections between the NCM particles. Thus, when more CB is used in the matrix, the probability of electronic connection of a NCM particle increases. For the 80:20:3 composition this leads to the highest achievable capacity of 129 mAh g⁻¹ at low C-rates (see also Supplementary Figure S15a, S16 and Table S4).

On the other hand, we observe that high CB contents are detrimental to the cell kinetics in this study. This is evident from the active specific capacities shown in Fig. 9b which are calculated by referring the measured charge only to the mass of active CAM. Hence, these capacity values describe the kinetics only of the statically active particles. For the 80:20:0.5 composition, an active specific capacity of 180 mAh g⁻¹ at 1C is obtained while for the 80:20:3 composition, only about 10 mAh g⁻¹ are reached. The differential capacity curves depicted in Fig. 9c for discharge cycles at 0.3C and 1C confirm the differences in kinetic performance depending on the CB content. This is further supported by Supplementary Figure S16 which shows that more charge is gained from the CV period for the samples with higher CB content, indicating available but kinetically limited capacity.

For an overall assessment, the active specific capacity values, representing a kinetic property, must be considered alongside CAM utilization, which reflects a static property³⁴: A high CB content increases the CAM utilization by providing more electronic pathways, leading to higher capacities at low C-rates. However, it simultaneously obstructs the ionic pathways, thereby impairing the kinetic cell performance resulting in low capacities at higher C-rates. Conversely, a low CB content reduces the static CAM utilization, with many CAM particles remaining electronically disconnected and thus electrochemically inactive. At the same time, the remaining electrochemically active particles are found to be kinetically well connected, which is reflected in the high active specific capacities at 1C (Fig. 9b) and lower overpotentials (Supplementary Figure S16). The improved kinetic performance during charging and discharging is further underlined by the fact that these particles experience a significantly higher effective C-rate due to the low CAM utilization.^{34,79} We do not observe a monotonic trend in capacity as a function of CB content, which we attribute to the fact that the CB distribution within the matrix coating is not yet fully optimized. Consequently, CB agglomeration may lead to reduced electronic connectivity, particularly at CB contents at or below the percolation threshold. This highlights the need to further optimize CB distribution in the matrix, which should be sufficient to ensure high CAM utilization, yet low enough to maintain fast transport kinetics and to prevent excessive electrochemical SE degradation.

In order to quantify the impact of chemo-mechanical degradation, *i.e.*, contact loss,^{27,33} during cycling at 1C in CCCV mode, the CAM utilization was determined every 20 cycles. Fig. 9d indicates that contact loss, which results in loss of active mass, is more pronounced for the cells with high CB content. We hypothesize that the observed behavior stems from the mechanical properties of the matrix. With increasing CB content, the matrix is much more porous, exhibits reduced elasticity, and shows a greater tendency toward plastic deformation which may hinder its

ability to accommodate the volume changes of NCM during continuous cycling. In contrast, a matrix with low CB content is more elastic and maintains contact with the NCM during cycling. For these composites the CAM utilization slightly increases and appears to stabilize during cycling, indicating microstructural changes which lead to new electronic connections.

Nanoindentation measurements on the CB-LIC premix (Supplementary Figure S17), from which we calculated the elastic and plastic portions of the indentation response (Fig. 9e), corroborate this picture. While there is approximately 20 % plastic portion at 2.5 wt.% CB in the matrix, it rises to around 50 % at 15 wt.% CB, highlighting a substantial shift toward plasticity at higher CB concentrations. This behavior is accompanied by a substantial rise in porosity of the CB-LIC matrix with increasing CB content (Supplementary Figure S17). Notably, at CB contents of 10 % and 15 % in the matrix, the porosity increases sharply from below 5 % (at low CB levels) to approximately 25 % and 30 %, respectively. The pronounced increase in porosity is directly linked with the observed rise in plasticity and correlates with the sharp decline in CAM utilization during long-term cycling at high CB contents in the coating. As the matrix becomes mechanically less elastic, it loses its ability to accommodate microstructural changes, such as the volume expansion of the CAM, during cycling, leading to significant contact losses and degradation in electrochemical performance (Fig. 9f).

Overall, our results reveal a trade-off between CAM utilization, charge transport kinetics, and mechanical integrity, with a composition of 80:20:0.5 leading to the best performance among the compositions tested in this study. Thereby, no direct correlation between the partial conductivities and half-cell performance is found. The results indicate that the percolation threshold value determined in a macroscopic measurement is rather too high and leads to poor ionic conduction as well as unfavorable mechanical properties which results in a worsened half-cell performance. In general, the concept of partial conductivities appears to have limited meaning

in the context of the mixed conducting matrix coating approach introduced in this study. Especially mechanical properties and porosity of the CB-LIC premix as well as the interfacial contact quality are not reflected in these measurements although they were shown to play a significant role. A more relevant assessment can be made by distinguishing between static and kinetic capacity losses in half-cell performances during cycling.

3. Discussion

Interfacial engineering remains a key challenge for SSBs, as electrochemical, chemical, and especially mechanical instabilities at interfaces strongly affect cycling stability and rate performance. Among various mitigation strategies, solution-based and mechanochemical coating routes have emerged as two complementary approaches to optimize SSB microstructures.

Solution-based routes may enable the formation of SEs around CAM particles in-situ. For the halide SE Li_3InCl_6 , such coatings have been demonstrated for LiCoO_2 by Wang *et al.*⁸⁰ and Ma *et al.*⁸¹ using aqueous precursor solutions, followed by (freeze-)drying to crystallize the coating phase. This one-step route is attractive for scalability and energy efficiency, since no separate SE synthesis is required. However, aqueous processing is limited to water-tolerant CAMs like LiCoO_2 , as Ni-rich CAMs can degrade upon water exposure.⁸²⁻⁸⁴ To date, water-based synthesis has only been reported for Li_3InCl_6 ⁸⁵, while other halide SEs and especially sulfide SEs, are chemically unstable in water or alcohols.^{55,86,87} Consequently, toxic or highly flammable solvents such as xylene, toluene, or acetonitrile are required.⁸⁸⁻⁹¹ This introduces safety risks and higher processing costs due to significant energy demand for solvent evaporation and recovery.

Mechanochemical coatings, as presented in this study, offer a solvent-free alternative avoiding interactions of the solvent with the CAM. High-shear mixing deposits pre-synthesized SEs directly onto CAMs, ensuring intimate contact and large interfacial area without SE pre-

comminution or drying steps.^{60,61,63,65} Pre-synthesized SE powders (e.g. LIC or sulfides) are mechanically attached to CAM particles without any intensive SE particle pre-comminution or drying step, eliminating solvent use and associated environmental and safety concerns. Although SE pre-synthesis is still needed, advances in large-scale mechanochemical synthesis have reduced its energy demand,^{15,92} potentially enabling a fully solvent-free SSB manufacturing chain.⁷⁶

As shown in this work, coating formation and homogeneity in dry mechanofusion processes are governed by the interplay between various process parameters, requiring precise process optimization. Excessive collision intensities can induce mechanical degradation of the CAM or SE,⁷⁶ while insufficient stress intensity and/or number leads to incomplete coatings. The risk of particle defects or breakage increases for large or polycrystalline CAMs due to their higher defect probability. Conversely, small, single-crystalline CAM particles exhibit superior mechanical stability, which explains why no measurable degradation was observed even at the highest stress intensities (10,000 rpm, 60 min) within the mixer used in this study. Further performance improvement is expected by optimizing the homogeneous dispersion of CB in the matrix.⁹³⁻⁹⁵ In particular, preventing agglomeration of the conductive additive should enhance CAM utilization while preserving fast interfacial charge transfer and transport throughout the composite cathode. Since both mechanochemical and solution-based coating strategies have distinct advantages and limitations, their applicability will depend on the specific material system, thereby motivating further process optimization and degradation studies.

In summary, we demonstrate that high-intensity mixing leading to mechanofusion is a promising well scalable dry-processing approach to fabricate tailored microstructures. We exploit the plastic deformability of Li_3InCl_6 as a model solid electrolyte, to create nanometer-thin coatings on the one hand, while also being suitable for building up well defined thicker mixed conducting matrix coatings around single-crystalline NCM on the other. The process can be broadly applied

across different type of solid electrolytes. Unlike simple mixing of loose particles and arbitrary (re-)ordering, the mechanofusion process offers a bottom-up pathway to engineer cathode building blocks with good interfacial connectivity, eliminating the need for manual mixing or multiple post-processing steps. Through systematic variation of process conditions and compositions, supported by DEM simulations and advanced analytics, we identified key parameters controlling the coating morphology, quantified by XPS-derived coverage values, and electrochemical performance. Notably, cathodes with a composition of 80:20:0.5 (NCM:LIC:CB, w/w/w) exhibited stable cycling at 1C and a specific capacity of $q_{\text{comp}}=100 \text{ mAh g}^{-1}$, calculated with respect to the total mass of the composite cathode. We expect considerably higher capacities once solid electrolytes with much higher conductivity in the order of 10 mS cm^{-1} will be used. Our findings indicate a clear trade-off between CAM utilization, cell kinetics at higher CB contents, and mechanical behavior of the matrix coating, underlining the importance of optimizing the composite mixing process. Overall, this work presents a promising and scalable strategy for advancing the manufacturing of high-performance SSB cathodes. While also discussing corresponding challenges of this approach, it motivates further exploration of engineered particle architectures in solid state energy storage systems.

4. Methods

Materials

Single-crystalline NCM82 ($\text{LiNi}_{0.82}\text{Mn}_{0.07}\text{Co}_{0.11}\text{O}_2$ from MSE Supplies, Tucson, AZ, USA), carbon black (Super C65 from Imerys, France) and in-house synthesized Li_3InCl_6 (LIC) were used. For the latter one a water-mediated synthesis carried out in a dried room with a dew point of $-60 \text{ }^\circ\text{C}$. The starting components LiCl (99%, Fisher Scientific, Waltham, MA, USA) and InCl_3 (99.995%, Fisher Scientific, Waltham, MA, USA) with a mass ratio of 0.365:0.635 (LiCl:InCl₃) were mixed

in deionized water at 40 °C for 2 h using a stir fish. Then, the mixture was first dried at 80 °C with the vessel open for 24 h and afterwards dried under vacuum for 4 h at 200 °C. From each batch, 32 g of dried in-house synthesized LIC was obtained, and this water-mediated synthesis route could be easily scaled up by employing larger vessels. After drying, the LIC was comminuted using a planetary ball mill (Pulverisette 7, Fritsch GmbH, Idar-Oberstein, Germany) at 600 rpm for 4 minutes with 5 mm ZrO₂ milling beads, using a 50 % milling bead filling ratio.

High-intensity mixing

The building blocks were produced using a Picoline high-intensity mixer equipped with a Nobilta attachment (Hosokawa Alpine AG). Mixing was performed in a dry room maintained at a dew point of -60 °C of the supply air. To mitigate the considerable heat generated during mixing, continuous cooling was applied. The material volume that was filled in was consistently set to 4.91 mL based on the calculated pure mixed density ρ_{mix} across all tests to ensure comparability of stressing conditions (cf. Table S1). In the CB-containing samples, CB and LIC were premixed at 5,000 rpm for 10 minutes to pre-structure the matrix coating. NCM was subsequently added, and mixing was continued for up to 60 minutes. Sampling during the rotational speed variation tests was performed at 5, 10, 30, and 60 minutes. All mixtures were stored in sealed bags in an argon atmosphere within the dry room prior to further analysis.

Power data evaluation

The power data P of the high-intensity mixer was continuously recorded at 5 s intervals throughout the entire mixing process. For the evaluation of the experimental specific energy input $E_{\text{m,exp}}$, only the 60 minute mixing phase of all three components was considered. To smooth the power signal, a Savitzky-Golay filter with a span of 50 data points was applied. The idle power P_0 corresponding

to each rotational speed was subsequently subtracted from the smoothed data. The resulting net power ΔP was then normalized to the mass of the composite m_{total} used in each experiment (cf. Table S1). Finally, the experimentally derived specific energy input $E_{\text{m,exp}}$ was calculated with the corresponding mixing time t_{mix} according to Equation 3.

$$E_{\text{m,exp}} = \frac{\sum_0^{t_{\text{mix}}} \Delta P \cdot \Delta t}{m_{\text{total}}} \quad 3$$

Particle size analysis

To determine the particle size of the building blocks, three SEM images were analyzed using an in-house artificial intelligence tool (particleOS.AI). Details are found in Supplementary Note 1.

DEM Simulations

Coarse-grained DEM simulations were conducted to capture the macroscopic processing conditions inside the high-intensity mixing device using Rocky version 2024 R1. To reduce computational cost and enable simulations within a practical timeframe, the particle size was coarse-grained to 300 μm , approximately 100 times larger than the actual experimental particle size.

Calibration experiments and simulations were performed to reproduce the particle dynamics and material behavior. First, compaction experiments were carried out using a ZWICK materials testing machine (ZwickRoell GmbH & Co. KG, Ulm, Germany). In these tests, 1 g of the 80:20:3 composite (processed at different rotational speeds for 60 min) was compacted up to 1000 N, and the corresponding force-displacement curves were recorded. In the DEM simulations, an equivalent 1 g of coarse-grained particles was placed inside a virtual compaction cylinder and

compressed until a force of 1000 N and the same average displacement as in the experiments were reached. By adjusting the yield ratio, Young's modulus, and friction parameters, the mechanical response of the simulated particles was calibrated to match the experimental results (cf. Supplementary Figure S10a).

To further capture the particle flow behavior, the dynamic angle of repose of the 80:20:3 composition was determined using a GranuDrum (Granutools, Awans, Belgium) at a rotational speed of 20 rpm and 51.2 g of powder, during which 60 images were recorded and averaged. In the simulations, a corresponding slice of the drum was modeled and filled with coarse-grained particles rotated at the same speed. As only 15 % of the drum length was simulated, only 7.68 g of coarse-grains were used in the simulation to save computation time. The static and dynamic friction coefficients were then iteratively adjusted to reproduce the experimentally observed angle of repose (cf. Supplementary Figure S10b). The set of calibrated parameters used in the simulation is provided in Supplementary Table S2.

The coarse-grained particles were assumed to possess an internal porosity of 0.39. Based on an experimentally determined bulk density of 1.45 g cm^{-3} and a theoretical mixed density of 3.94 g cm^{-3} for the 80:20:3 composition, a corresponding coarse-grain density of 2.417 g cm^{-3} was calculated (cf. Supplementary Figure S10c). To validate this value, the filling volume determined from the GranuDrum experiments was compared with the simulated filling volume, showing a high agreement (cf. Supplementary Figure S10d).

To replicate the 80:20:3 mixing experiment at different rotational speeds, the mixing chamber of the high-intensity mixer was virtually filled with 3.88 g of material (one-fifth of the material) via two particle inlets over a time span of 0 s to 0.1 s., and only one-fifth of the mixer volume was simulated, following the approach by Frankenberg *et al.*⁴³ Following the filling phase, the rotor was set to rotate at varying speeds for 0.4 s until the steady state was reached. The

mechanical power acting on the rotor was computed and compared to the experimentally recorded net power, enabling validation of the calibration of the simulation parameters from the compaction and angle of repose experiments. The elasto-plastic Thornton–Ning contact model was employed to account for both the plasticity and elasticity of the particle species.

In addition to the overall power acting on the rotor, particle-based (*i*) mean dissipated power \overline{P}_i^α was extracted during the output intervals of $\Delta t_{\text{out}} = 0.005$ s and evaluated following the methodology described by Frankenberg *et al.*⁴³ Therefore, the power values, which are a sum of the work done at one particle $\sum_{c=1}^{N_{c,i}} W_c^{\text{diss}}$ during the output interval, was divided by its collision frequency $c_i = \frac{\Delta t_{\text{out}}}{N_{c,i}}$ and the mass of one coarse-grain particle $m_{\text{particle,CG}}$ to obtain particle-based stress intensities. These stress intensities for each output interval were stored $N_{c,i}$ times to consider that particles undergo $N_{c,i}$ collisions during the output interval. From this data, stress intensity *SI* - stress frequency relationships were derived and the overall mean stress intensity $\overline{SI}_{\text{CG}}$ of this distribution as well as the coarse-grain stress frequency SF_{CG} representing the number of all coarse-grain collision events of all particles per second were derived. The stress number per particle \overline{SN}_p , corresponding to the total number of stress events per particle over the process time, was then calculated by integrating the stress frequency over time⁴³.

$$\overline{SI}_{\text{CG},i}^{\text{diss}} = \frac{P_i^{\text{diss}}}{c_i \cdot m_{\text{particle,CG}}} = \frac{\sum_{c=1}^{N_{c,i}} W_c^{\text{diss}}}{\Delta t_{\text{out}}} \cdot \frac{\Delta t_{\text{out}}}{N_{c,i}} \cdot \frac{1}{m_{\text{particle,CG}}} \quad 4$$

$$\overline{SN}_p = SF_{\text{CG}} \cdot t_{\text{mix}} \cdot \frac{m_{\text{particle,CG}}}{m_{\text{total}}} \quad 5$$

XRD analysis

X-ray diffraction (XRD) patterns were recorded using a diffractometer equipped with a Cu $K\alpha$ monochromatic source ($\lambda = 0.154$ nm; Empyrean, Malvern Panalytical, Kassel, Germany).

Measurements were performed over an angular range of 5° to 120° 2θ with a step size of 0.053° 2θ . Samples were prepared in an argon atmosphere and sealed with kapton foil to prevent air exposure during analysis. Background subtraction was applied to all spectra.

Additional XRD measurements to determine the influence of the mixing process on micro-strain were performed using a diffractometer equipped with a Mo K_α source ($= 0.071$ nm; Empyrean, Malvern Panalytical, Kassel, Germany). Measurements were performed over an angular range of 5° to 40° with a step size of 0.053° using capillaries with 0.6 mm diameter in transmission mode and divergent beam path. Samples were prepared in an argon atmosphere.

Nanoindentation

Nanoindentation measurements were carried out on pellets made from CB-LIC premixes with varying compositions. The pellets were prepared by compressing 0.69 g of premix at 380 MPa for 3 minutes using a laboratory press (LaboPress P200S, Vogt Labormaschinen, Germany). Each pellet was then affixed to a glass slide using epoxy resin. To protect the sample from air exposure during transfer, a plastic collar was mounted around the pellet, and a glass cover slip was sealed on top with high-viscosity paste.

Measurements were conducted using a TriboIndenter system (Hysitron Inc., Minneapolis, MN). The sample chamber was purged with argon prior to testing to prevent degradation of the pellet. A $100\ \mu\text{m}$ diameter flat punch indenter was used in displacement-controlled mode. Indentations were performed to a depth of $10\ \mu\text{m}$ at a loading rate of $500\ \text{nm s}^{-1}$. For each pellet, 25 indentations were made, and the average force–displacement curve was determined. From the curves, both the elastic W_{elastic} and plastic W_{plastic} work portions of the total indentation work W_{total} were quantified.

$$W_{\text{total}} = \int_0^{s_{\text{max}}} F_{\text{loading}}(s) ds \quad 6$$

$$W_{\text{elastic}} = \int_{s_0}^{s_{\text{max}}} F_{\text{unloading}}(s) ds \quad 7$$

$$W_{\text{plastic}} = W_{\text{total}} - W_{\text{elastic}} \quad 8$$

Here, s_{max} denotes the maximum indentation depth at the highest applied load, while s_0 corresponds to the residual indentation depth after unloading (i.e., the intersection with the x -axis). F_{loading} and $F_{\text{unloading}}$ represent the measured force during the loading and unloading phases, respectively.

Determination of porosity

The porosity of the composites and pure materials was measured in a slightly compacted state using a ZWICK materials testing machine (ZwickRoell GmbH & Co. KG, Ulm, Germany). For each sample, three measurements were performed by filling 1 g of composite powder into the measuring cylinder of the instrument. For the individual raw materials, the following masses were used: 2 g for LIC, 0.25 g for CB, and 1 g for NCM. Compaction was performed up to a force of 395 N (3.45 MPa), and the displacement and applied force were recorded. The bulk density ρ_{bulk} of the composite was determined geometrically in the compacted state, and porosity ε was calculated based on the mixed theoretical solids density ρ_{mix} derived from the known raw material densities, which are $\rho_{\text{NCM}}=4.75 \text{ g cm}^{-3}$, $\rho_{\text{LIC}}=2.59 \text{ g cm}^{-3}$ and $\rho_{\text{CB}}=1.96 \text{ g cm}^{-3}$ (cf. Table S1).

$$\rho_{\text{mix}} = \text{vol. \%}_{\text{NCM}} \cdot \rho_{\text{NCM}} + \text{vol. \%}_{\text{LIC}} \cdot \rho_{\text{LIC}} + \text{vol. \%}_{\text{CB}} \cdot \rho_{\text{CB}} \quad 9$$

$$\varepsilon = 1 - \frac{\rho_{\text{bulk}}}{\rho_{\text{mix}}} \quad 10$$

The porosity of the CB-LIC pellets used for nanoindentation measurements was determined after compaction at 380 MPa.

Scanning electron microscopy (SEM)

The sample preparation was performed in an argon-filled glovebox with oxygen residues of $p(\text{O}_2)/p < 1.0$ ppm and water residues of $p(\text{H}_2\text{O})/p < 1.0$ ppm. The particles were imaged using a field-emission SEM *GeminiSEM 560* system (Carl Zeiss Microscopy GmbH, Jena, Germany) with 2 kV acceleration voltage and 3 mm working distance. EDX analysis was carried out with the *AzTec* EDX system (Oxford Instruments, United Kingdom). EDX mapping was performed with an acceleration voltage of 10 kV at a working distance of 8.5 mm using the *Ultim Max* detector. Prior to imaging, the particles were sputtered with a 4 nm thin layer of platinum using a LEICA EM ACE600 coater (Leica Microsystems GmbH, Wetzlar, Germany).

(Scanning) Transmission Electron Microscopy ((S)TEM)

The sample preparation of the powder sample was performed in an argon-filled glovebox with oxygen residues of $p(\text{O}_2)/p < 1.0$ ppm and water residues of $p(\text{H}_2\text{O})/p < 1.0$ ppm. Here, the particles were spread onto carbon film-coated Cu-mesh TEM grids. Moreover, a TEM lamella was prepared by focused ion beam (FIB) milling using a HeliosTM 5 Hydra CX DualBeam System (Thermo Fisher Scientific Inc.). The sample was transferred in argon atmosphere from the glove box to the FIB system and back using the CleanConnect inert gas transfer system. The TEM grids were then loaded in the glovebox into an inert gas/vacuum transfer TEM holder (from Mel-Build) to avoid reaction of the samples with humidity in the air and transferred to a pumping stand. Here, the argon inside the holder was removed before inserting the holder into the TEM.

High-resolution as well as bright-field and dark-field TEM images were recorded on both a JEOL JEM 3010 (300 kV) and a double Cs-corrected JEOL JEM 2200 FS (200 kV). Both microscopes are equipped with a TVIPS TemCam XF416FS camera, which was used for image acquisition.

The SPED phase map was measured on the JEOL JEM 3010 equipped with a NanoMEGAS P2000 ASTAR system for scanning and precessing the beam (precession angle 0.6°). The four-dimensional data set was recorded with the TVIPS TemCam XF416FS camera as a video, which was later converted into a rectangular data set (.bloc format) using an in-house written Python code and evaluated using the NanoMEGAS software suite DiffGen 2, Index 2, and MapViewer 2. For phase matching, the crystallographic files (.cif) for NCM82, NiO, and LIC taken from the Inorganic Crystal Structure Database (ICSD) were used as input.

EDX data was recorded on the JEOL JEM 2200 FS using a Bruker Nano XFlash Detector 5060 in scanning TEM mode with a semi-convergence angle of 15.07 mrad. The map data was evaluated using the Esprit 2.3 software.

X-ray Photoelectron Spectroscopy (XPS)

XPS analysis was performed using a PHI Versa Probe IV system (Physical Electronics Inc., Chanhassen, MN, USA). The powders were filled into Teflon crucibles (inner diameter: 3 mm), pressed to achieve a flat surface and attached to the sample holder using nonconductive adhesive tape. The sample preparation was performed in an argon-filled glovebox with oxygen residues of $p(\text{O}_2)/p < 1.0$ ppm and water residues of $p(\text{H}_2\text{O})/p < 1.0$ ppm. All samples were transferred to the XPS machine in an air-tight transfer vessel. Monochromatic Al- K_α radiation (1486.6 eV) was applied for XPS analysis. The X-ray source was operated at a power of 50 W and a voltage of 15 kV having a beam diameter of 200 μm . A pass energy of 55 eV, a step size of 0.2 eV, a step time of

25 ms and 20 sweeps were used. The samples were charge-neutralized during measurements. The XPS data were evaluated using CasaXPS (Casa Software Ltd., Teignmouth, UK). The spectra were calibrated in relation to the signal of adventitious carbon C 1s at 284.8 eV. For each detail spectrum, a region with the same energy boundaries was defined and the respective intensities I_{element} (in CPS) were used to calculate the coverage values γ ⁶⁶:

$$\gamma = \frac{I_{\text{Cl}} + I_{\text{In}}}{I_{\text{Cl}} + I_{\text{In}} + I_{\text{Ni}} + I_{\text{Mn}}} \quad 11$$

Equation 11 does not contain the C 1s signal intensity because this would include signal intensity stemming from adventitious carbon which cannot be distinguished from the CB contribution. Moreover, the overall signal intensity, including C 1s, depends on several experimental parameters and shows noticeable variations between nominally similar samples. Thus, even the corrected C 1s intensity, obtained by subtraction the C 1s intensity of a CB-free reference sample, was not used in the coverage calculation. XPS-derived coverage values close to 1 reflect that a covering, >10 nm thick, coating layer was achieved. The values contain no information on the morphology and exact thickness distribution. The coverage values contain averaged information over more than 1000 particles.

Cell building and electrochemical evaluation

All electrochemical cells were built in an argon-filled glovebox with oxygen residues of $p(\text{O}_2)/p < 1.0$ ppm and water residues of $p(\text{H}_2\text{O})/p < 1.0$ ppm. The cell components were filled in an in-house built cell casing containing a PEEK die with an inner diameter of 10 mm.³⁴ The electrochemical measurements were carried out in a controlled environment at $T = 25$ °C. During all electrochemical measurements, the cells were fixed in a steel frame while applying a pressure of approximately 80 MPa (10 Nm torque).

For the determination of the effective partial electronic conductivity, symmetric ion-blocking cells were used with stainless steel rods serving as contacts. 120 mg of the matrix and composite powders were compacted with an uniaxial pressure of 380 MPa for 3 min at room temperature.

For the determination of the effective partial ionic conductivity, symmetric electron-blocking cells were used. For this purpose, 240 mg of composite was hand-pressed and then 60 mg of $\text{Li}_6\text{PS}_5\text{Cl}$ (LPSCI, *Argyrodite-CMP5* from Posco JK Solid Solution, South Korea) was added to each side. The three layers were compacted with a uniaxial pressure of 380 MPa for 3 min at room temperature. Then, indium foil (99.999 %, 100 μm thickness, 9 mm diameter, Chempur, Germany) and lithium foil (100 μm thickness, 4 mm diameter, China Energy Lithium), were pressed together on both sides to serve as lithium reservoirs.

For the experimental measurement of effective partial conductivities, chronoamperometry was applied until a stable steady-state current was reached at every voltage step. The voltage-current tuples were fitted linearly, and the resistance and the corresponding conductivity were evaluated according to Ohm's law. For the symmetric electron-blocking cells, an additional reference measurement using Li-In|LPSCI|In-Li was carried out. The associated resistance was subtracted from the total resistance before calculating the ionic partial conductivity.

For the half-cell testing in a in-house made cell casing⁹⁶, the following setups was used: First, 40 mg of LPSCI powder (*Argyrodite-CMP5* from Posco JK Solid Solution, South Korea) was evenly filled in a PEEK cylinder (10 mm diameter) and pressed by hand. Subsequently, a layer of 40 mg LIC was added and also hand pressed, completing the bilayer separator⁹⁷. Then, approximately 15 mg of the cathode composite was evenly distributed on the LIC layer. On the LPSCI layer of the bilayer separator, an indium foil (99.999%, 100 μm thickness, 9 mm diameter, Chempur, Germany) and a lithium foil (100 μm thickness, 6 mm diameter, China Energy Lithium)

were placed to form the In/InLi anode. Afterwards, the cell was uniaxially pressed with approximately 380 MPa for 3 minutes while being isolated.

The cells were cycled in a cell voltage range between 2.0 and 3.7 V vs. In/InLi at room temperature using a BCS-805 Battery Cycling System (Bio-Logic, Seyssinet-Pariset, France) and a MACCOR electrochemical workstation. Charging was done in CCCV mode by holding the cutoff potential for 1 h. The C-rates were calculated based on a CAM specific capacity of 200 mAh/g_{NCM} taking into account the nominal amount of NCM in the cathode (1C \approx 200 mA/g \approx 3 mA/cm²).

The CAM utilization was determined similar to as described in a previous publication³⁴. Each SSB cell was charged with 0.1C to 3.1 V vs. In/InLi, held at that potential for 3 h, followed by 3 h of relaxation to determine the potential V_1 . Then, the cell was charged with 0.05C up to 3.4 V, followed by 5 h of relaxation to get the potential V_2 . The relaxed OCP values are given in the Supplementary Source Data File. As a quasi-OCP (titration) curve of the CAM, the capacity-voltage curve of a liquid electrolyte cell at 0.02C was taken as a reference (cf. Supplementary Figure S18) for which the data file is openly available in Zenodo at <https://doi.org/10.5281/zenodo.14065128>, reference number 14065128. For the LIB reference cell, it was assumed that it possesses a comparable voltage-capacity curve as the SSBs. The validity of this approximation is discussed in Supplementary Figure S19.

The liquid cell data was used to assign a reference specific capacity value $q_{\text{ref,LIB}}$ to the potential range determined by V_1 and V_2 . This value was compared with the measured capacity q_{measured} of the solid state cell, which can be extracted with the analysis software. The CAM utilization was then calculated with Equation 11:

$$\text{CAM Utilization} = \frac{q_{\text{measured}}}{q_{\text{ref,LIB}}} \quad 12$$

The active specific capacities are calculated by dividing the measured capacities by the CAM utilization, *i.e.*, the charge is referred only to the actual electrochemically active mass.

Data availability

The source data used for all figures in this study are provided in the Source Data File, which has been deposited, together with additional data, in Zenodo at <https://doi.org/10.5281/zenodo.18493074>.

References

1. Janek, J. & Zeier, W. G. A solid future for battery development. *Nat Energy* **1** (2016).
2. Alex M. Bates *et al.* Are solid-state batteries safer than lithium-ion batteries? *Joule* **6**, 742–755 (2022).
3. Wang, R., Cui, W., Chu, F. & Wu, F. Lithium metal anodes: Present and future. *Journal of Energy Chemistry* **48**, 145–159 (2020).
4. Huang, W.-Z. *et al.* Anode - Free Solid - State Lithium Batteries: A Review. *Adv. Energy Mater.* **12** (2022).
5. Song, A. *et al.* A Review on the Features and Progress of Silicon Anodes - Based Solid - State Batteries. *Adv. Energy Mater.* **13** (2023).
6. Janek, J. & Zeier, W. G. Challenges in speeding up solid-state battery development. *Nat Energy* **8**, 230–240 (2023).
7. Minnmann, P. *et al.* Designing Cathodes and Cathode Active Materials for Solid - State Batteries. *Advanced Energy Materials* **12** (2022).
8. Dixit, M. B. *et al.* Understanding implications of cathode architecture on energy density of solid-state batteries. *Energy Storage Materials* **40**, 239–249 (2021).
9. Han, Y. *et al.* Single - or Poly - Crystalline Ni - Rich Layered Cathode, Sulfide or Halide Solid Electrolyte: Which Will be the Winners for All - Solid - State Batteries? *Advanced Energy Materials* **11**, 2100126 (2021).
10. Kamaya, N. *et al.* A lithium superionic conductor. *Nature materials* **10**, 682–686 (2011).
11. Kuhn, A. *et al.* A new ultrafast superionic Li-conductor: ion dynamics in $\text{Li}_{11}\text{Si}_2\text{PS}_{12}$ and comparison with other tetragonal LGPS-type electrolytes. *Physical chemistry chemical physics : PCCP* **16**, 14669–14674 (2014).
12. Wang, Z.-Y. *et al.* Achieving high-energy and high-safety lithium metal batteries with high-voltage-stable solid electrolytes. *Matter* **6**, 1096–1124 (2023).

13. Liu, J., Wang, S., Qie, Y. & Sun, Q. Identifying lithium fluorides for promising solid-state electrolyte and coating material of high-voltage cathode. *Materials Today Energy* **21**, 100719 (2021).
14. Dai, T. *et al.* Inorganic glass electrolytes with polymer-like viscoelasticity. *Nature Energy* **8**, 1221–1228 (2023).
15. Grube, M. *et al.* Solvent-free and scalable mechanochemical synthesis of high-performance sulfide solid electrolytes. *Journal of Energy Storage* **121**, 116593 (2025).
16. Jo, Y.-S. *et al.* Engineering green and sustainable solvents for scalable wet synthesis of sulfide electrolytes in high-energy-density all-solid-state batteries. *Green Chem.* **25**, 1473–1487 (2023).
17. Kimura, Y. *et al.* Coating layer design principles considering lithium chemical potential distribution within solid electrolytes of solid-state batteries. *Commun Mater* **5**, 1–13 (2024).
18. Nakamura, T., Amezawa, K., Kulisch, J., Zeier, W. G. & Janek, J. Guidelines for All-Solid-State Battery Design and Electrode Buffer Layers Based on Chemical Potential Profile Calculation. *ACS Applied Materials and Interfaces* **11**, 19968–19976 (2019).
19. Ruess, R. *et al.* Single-Crystalline LiNiO₂ as High-Capacity Cathode Active Material for Solid-State Lithium-Ion Batteries. *J. Electrochem. Soc.* **170**, 20533 (2023).
20. Wang, L. *et al.* High-energy all-solid-state lithium batteries enabled by Co-free LiNiO₂ cathodes with robust outside-in structures. *Nat. Nanotechnol.* **19**, 208–218 (2024).
21. Dai, Y. *et al.* Exploring of the upper limit of nickel content in cathode materials for PEO-based solid-state batteries. *Chinese Chemical Letters*, 111157 (2025).
22. Strauss, F. *et al.* Rational Design of Quasi-Zero-Strain NCM Cathode Materials for Minimizing Volume Change Effects in All-Solid-State Batteries. *ACS Materials Lett.* **2**, 84–88 (2020).
23. Liu, C., Roters, F. & Raabe, D. Role of grain-level chemo-mechanics in composite cathode degradation of solid-state lithium batteries. *Nature communications* **15**, 7970 (2024).
24. Koerver, R. *et al.* Chemo-mechanical expansion of lithium electrode materials – on the route to mechanically optimized all-solid-state batteries. *Energy & Environmental Science* **11**, 2142–2158 (2018).
25. Ryu, H.-H. *et al.* Microstrain Alleviation in High-Energy Ni-Rich NCMA Cathode for Long Battery Life. *ACS Energy Lett.* **6**, 216–223 (2021).
26. Kondrakov, A. O. *et al.* Anisotropic Lattice Strain and Mechanical Degradation of High- and Low-Nickel NCM Cathode Materials for Li-Ion Batteries. *J. Phys. Chem. C* **121**, 3286–3294 (2017).
27. Conforto, G. *et al.* Editors' Choice—Quantification of the Impact of Chemo-Mechanical Degradation on the Performance and Cycling Stability of NCM-Based Cathodes in Solid-State Li-Ion Batteries. *J. Electrochem. Soc.* **168**, 70546 (2021).
28. Payandeh, S., Goonetilleke, D., Bianchini, M., Janek, J. & Brezesinski, T. Single versus poly-crystalline layered oxide cathode materials for solid-state battery applications - a short review article. *Current Opinion in Electrochemistry* **31**, 100877 (2022).

29. Raffael Ruess *et al.* Influence of NCM Particle Cracking on Kinetics of Lithium-Ion Batteries with Liquid or Solid Electrolyte. *Journal of The Electrochemical Society* **167**, 100532 (2020).
30. Trevisanello, E., Ruess, R., Conforto, G., Richter, F. H. & Janek, J. Polycrystalline and Single Crystalline NCM Cathode Materials—Quantifying Particle Cracking, Active Surface Area, and Lithium Diffusion. *Advanced Energy Materials* **11**, 2003400 (2021).
31. Bielefeld, A., Weber, D. A. & Janek, J. Microstructural Modeling of Composite Cathodes for All-Solid-State Batteries. *Journal of Physical Chemistry C* **123**, 1626–1634 (2019).
32. Bielefeld, A., Weber, D. A., Rueß, R., Glavas, V. & Janek, J. Influence of Lithium Ion Kinetics, Particle Morphology and Voids on the Electrochemical Performance of Composite Cathodes for All-Solid-State Batteries. *J. Electrochem. Soc.* **169**, 20539 (2022).
33. Minnmann, P. *et al.* Editors' Choice—Visualizing the Impact of the Composite Cathode Microstructure and Porosity on Solid-State Battery Performance. *J. Electrochem. Soc.* **171**, 60514 (2024).
34. Kissel, M. *et al.* Quantifying the Impact of Cathode Composite Mixing Quality on Active Mass Utilization and Reproducibility of Solid - State Battery Cells. *Advanced Energy Materials* **15**, 2405405 (2025).
35. Minnmann, P., Quillman, L., Burkhardt, S., Richter, F. H. & Janek, J. Editors' Choice—Quantifying the Impact of Charge Transport Bottlenecks in Composite Cathodes of All-Solid-State Batteries. *J. Electrochem. Soc.* **168**, 40537 (2021).
36. Hendriks, T. A., Lange, M. A., Kiens, E. M., Baeumer, C. & Zeier, W. G. Balancing Partial Ionic and Electronic Transport for Optimized Cathode Utilization of High - Voltage $\text{LiMn}_2\text{O}_4/\text{Li}_3\text{InCl}_6$ Solid - State Batteries. *Batteries & Supercaps* **6** (2023).
37. Kaiser, N. *et al.* Ion transport limitations in all-solid-state lithium battery electrodes containing a sulfide-based electrolyte. *Journal of Power Sources* **396**, 175–181 (2018).
38. Bielefeld, A., Weber, D. A. & Janek, J. Modeling Effective Ionic Conductivity and Binder Influence in Composite Cathodes for All-Solid-State Batteries. *ACS Applied Materials and Interfaces* **12**, 12821–12833 (2020).
39. Kim, J. *et al.* High - Performance All - Solid - State Batteries Enabled by Intimate Interfacial Contact Between the Cathode and Sulfide - Based Solid Electrolytes. *Advanced Functional Materials* **33**, 2211355 (2023).
40. Lee, D. *et al.* Shear force effect of the dry process on cathode contact coverage in all-solid-state batteries. *Nature communications* **15**, 4763 (2024).
41. Schnell, J. *et al.* All-solid-state lithium-ion and lithium metal batteries – paving the way to large-scale production. *Journal of Power Sources* **382**, 160–175 (2018).
42. Batzer, M., Gundlach, D., Michalowski, P. & Kwade, A. Scalable Production of Separator and Cathode Suspensions via Extrusion for Sulfidic Solid - State Batteries. *ChemElectroChem* **10** (2023).
43. Frankenberg, F. *et al.* Investigating the production of all-solid-state battery composite cathodes by numerical simulation of the stressing conditions in a high-intensity mixer. *Powder Technology* **435**, 119403 (2024).

44. Noh, S., Nichols, W. T., Cho, M. & Shin, D. Importance of mixing protocol for enhanced performance of composite cathodes in all-solid-state batteries using sulfide solid electrolyte. *J Electroceram* **40**, 293–299 (2018).
45. Titscher, P., Götz von Olenhusen, A., Arlt, T., Manke, I. & Kwade, A. Evaluation of a High - Intensive Mixing Process in a Ring Shear Mixer and Its Impact on the Properties of Composite Particles for Lithium-Sulfur Battery Cathodes. *Energy Tech* **7** (2019).
46. Helmers, L. *et al.* Sustainable Solvent - Free Production and Resulting Performance of Polymer Electrolyte - Based All - Solid - State Battery Electrodes. *Energy Tech* **9** (2021).
47. Fernandez-Diaz, L. *et al.* Mixing methods for solid state electrodes: Techniques, fundamentals, recent advances, and perspectives. *Chemical Engineering Journal* **464**, 142469 (2023).
48. Puls, S. *et al.* Benchmarking the reproducibility of all-solid-state battery cell performance. *Nat Energy*, 1–11 (2024).
49. Maus, O. *et al.* Influence of Post - Synthesis Processing on the Structure, Transport, and Performance of the Solid Electrolyte $\text{Li}_{5.5}\text{PS}_{4.5}\text{Cl}_{1.5}$ in All - Solid - State Batteries. *Advanced Energy Materials* (2024).
50. Schlautmann, E. *et al.* Graded Cathode Design for Enhanced Performance of Sulfide-Based Solid-State Batteries. *ACS Energy Lett.*, 1664–1670 (2025).
51. Schlautmann, E. *et al.* Impact of the Solid Electrolyte Particle Size Distribution in Sulfide - Based Solid - State Battery Composites. *Advanced Energy Materials*, 2302309 (2023).
52. Shi, T. *et al.* High Active Material Loading in All - Solid - State Battery Electrode via Particle Size Optimization. *Advanced Energy Materials* **10**, 1902881 (2020).
53. König, C., Miß, V., Janin, L. & Roling, B. Mitigating the Ion Transport Tortuosity in Composite Cathodes of All-Solid-State Batteries by Wet Milling of the Solid Electrolyte Particles. *ACS Appl. Energy Mater.* **6**, 9356–9362 (2023).
54. Park, C. *et al.* Electrochemical Properties of Composite Cathode Using Bimodal Sized Electrolyte for All-Solid-State Batteries. *J. Electrochem. Soc.* **166**, A5318-A5322 (2019).
55. Ruhl, J., Riegger, L. M., Ghidui, M. & Zeier, W. G. Impact of Solvent Treatment of the Superionic Argyrodite $\text{Li}_6\text{PS}_5\text{Cl}$ on Solid - State Battery Performance. *Adv Energy Sustain Res* **2**, 2000077 (2021).
56. Wang, Y. *et al.* Mechanical Milling - Induced Microstructure Changes in Argyrodite LPSCl Solid - State Electrolyte Critically Affect Electrochemical Stability. *Advanced Energy Materials* (2024).
57. Choi, Y. E. *et al.* Coatable Li_4SnS_4 Solid Electrolytes Prepared from Aqueous Solutions for All-Solid-State Lithium-Ion Batteries. *ChemSusChem* **10**, 2605–2611 (2017).
58. Kim, D. H. *et al.* Infiltration of Solution-Processable Solid Electrolytes into Conventional Li-Ion-Battery Electrodes for All-Solid-State Li-Ion Batteries. *Nano letters* **17**, 3013–3020 (2017).
59. Lee, W. *et al.* Advanced parametrization for the production of high-energy solid-state lithium pouch cells containing polymer electrolytes. *Nat Commun* **15**, 5860 (2024).

60. Kawaguchi, T., Nakamura, H. & Watano, S. Dry coating of electrode particle with model particle of sulfide solid electrolytes for all-solid-state secondary battery. *Powder Technology* **323**, 581–587 (2018).
61. Kawaguchi, T., Nakamura, H. & Watano, S. Parametric study of dry coating process of electrode particle with model material of sulfide solid electrolytes for all-solid-state battery. *Powder Technology* **305**, 241–249 (2017).
62. Hayakawa, E., Nakamura, H., Ohsaki, S. & Watano, S. Dry mixing of cathode composite powder for all-solid-state batteries using a high-shear mixer. *Advanced Powder Technology* **33**, 103705 (2022).
63. Hayakawa, E., Nakamura, H., Ohsaki, S. & Watano, S. Design of active-material/solid-electrolyte composite particles with conductive additives for all-solid-state lithium-ion batteries. *Journal of Power Sources* **555**, 232379 (2023).
64. Friebel, J. M., Ditscherlein, R., Ditscherlein, L. & Peuker, U. A. Three-Dimensional Characterization of Dry Particle Coating Structures Originating from the Mechano-fusion Process. *Microscopy and microanalysis* **30**, 179–191 (2024).
65. Jin, F. *et al.* Elucidating the Impact of Li_3InCl_6 -Coated $\text{LiNi}_{0.8}\text{Co}_{0.15}\text{Al}_{0.05}\text{O}_2$ on the Electro-Chemo-Mechanics of $\text{Li}_6\text{PS}_5\text{Cl}$ -Based Solid-State Batteries. *Chem. Mater.* **36**, 6017–6026 (2024).
66. Kissel, M. *et al.* Engineering the Artificial Cathode-Electrolyte Interphase Coating for Solid-State Batteries via Tailored Annealing. *Chemistry of Materials* **37**, 2192–2203 (2025).
67. Kim, J. S. *et al.* Synergistic halide-sulfide hybrid solid electrolytes for Ni-rich cathodes design guided by digital twin for all-solid-State Li batteries. *Energy Storage Materials* **55**, 193–204 (2023).
68. Tanno, K. Current Status of the Mechanofusion Process for Producing Composite Particles. *KONA* **8**, 74–82 (1990).
69. Kwade, A. A Stressing Model for the Description and Optimization of Grinding Processes. *Chem Eng & Technol* **26**, 199–205 (2003).
70. Burmeister, C. F. & Kwade, A. Process engineering with planetary ball mills. *Chem. Soc. Rev.* **42**, 7660–7667 (2013).
71. Schlem, R. *et al.* Energy Storage Materials for Solid - State Batteries: Design by Mechanochemistry. *Adv. Energy Mater.* **11** (2021).
72. Burmeister, C. F., Hofer, M., Molaiyan, P., Michalowski, P. & Kwade, A. Characterization of Stressing Conditions in a High Energy Ball Mill by Discrete Element Simulations. *Processes* **10**, 692 (2022).
73. Zheng, L., Wei, C., Garayt, M. D. L., MacInnis, J. & Obrovac, M. N. Spherically Smooth Cathode Particles by Mechanofusion Processing. *J. Electrochem. Soc.* **166**, A2924-A2927 (2019).
74. Rumpf, H. C. H. Zur Theorie der Zugfestigkeit von Agglomeraten bei Kraftübertragung an Kontaktpunkten. *Chemie Ingenieur Technik* **42**, 538–540 (1970).
75. Tavares, L. & King, R. Single-particle fracture under impact loading. *International Journal of Mineral Processing* **54**, 1–28 (1998).

76. Frankenberg, F. *et al.* Tailoring Composite Microstructure Through Milling for Dry-Processed Sulfide-Based Solid-State Battery Cathodes. *Small (Weinheim an der Bergstrasse, Germany)* **21**, e07279 (2025).
77. Reisacher, E., Kaya, P. & Knoblauch, V. Percolation Behavior of a Sulfide Electrolyte–Carbon Additive Matrix for Composite Cathodes in All-Solid-State Batteries. *Batteries* **2019**, Vol. 5, Page 48 **9**, 595 (2023).
78. Puls, S., Ketter, L., Zeier, W. G. & Vargas-Barbosa, N. M. Opportunities and Limitations of Partial Transport Quantification in All-Solid-State Composite Electrodes. *ACS Electrochem.* (2025).
79. Yanev, S. *et al.* Rapid Determination of All-Solid-State Battery Performance via Chronoamperometry. *J. Electrochem. Soc.* **169**, 90519 (2022).
80. Wang, C. *et al.* Interface-assisted in-situ growth of halide electrolytes eliminating interfacial challenges of all-inorganic solid-state batteries. *Nano Energy* **76**, 105015 (2020).
81. Ma, T. *et al.* In-situ cathode coating for all-solid-state batteries by freeze-drying technology. *Nano Energy* **124**, 109522 (2024).
82. Mayer, J. K. *et al.* Investigation of Moisture Content, Structural and Electrochemical Properties of Nickel-Rich NCM Based Cathodes Processed at Ambient Atmosphere. *J. Electrochem. Soc.* **169**, 60512 (2022).
83. Lechner, M., Wölfl, S., Kurz, E. & Daub, R. Identification of critical moisture exposure for nickel-rich cathode active materials in lithium-ion battery production. *Journal of Power Sources* **626**, 235661 (2025).
84. Zhang, L. *et al.* Elucidating the Humidity-Induced Degradation of Ni-Rich Layered Cathodes for Li-Ion Batteries. *ACS applied materials & interfaces* **14**, 13240–13249 (2022).
85. Li, X. *et al.* Water - Mediated Synthesis of a Superionic Halide Solid Electrolyte. *Angew. Chem.* **131**, 16579–16584 (2019).
86. Zhang, Z. *et al.* One-step solution process toward formation of Li₆PS₅Cl argyrodite solid electrolyte for all-solid-state lithium-ion batteries. *Journal of Alloys and Compounds* **812**, 152103 (2020).
87. Nikodimos, Y., Huang, C. J., Taklu, B. W., Su, W. N. & Hwang, B. J. Chemical stability of sulfide solid-state electrolytes: stability toward humid air and compatibility with solvents and binders. *Energy & Environmental Science* **15**, 991–1033 (2022).
88. Park, K. H. *et al.* Design Strategies, Practical Considerations, and New Solution Processes of Sulfide Solid Electrolytes for All - Solid - State Batteries. *Advanced Energy Materials* **8** (2018).
89. Emley, B. *et al.* On the quality of tape-cast thin films of sulfide electrolytes for solid-state batteries. *Materials Today Physics* **18**, 100397 (2021).
90. Nikodimos, Y. *et al.* Unveiling the Chemical Stability and Solvent Compatibility of Halide Solid-State Electrolytes: Insights from Isothermal Calorimetric Titration and Synchrotron Spectroscopy. *Chem. Mater.* **37**, 7622–7634 (2025).
91. Wang, C. *et al.* A universal wet-chemistry synthesis of solid-state halide electrolytes for all-solid-state lithium-metal batteries. *Science Advances* **7** (2021).

92. Hofer, M. *et al.* Effective mechanochemical synthesis of sulfide solid electrolyte Li_3PS_4 in a high energy ball mill by process investigation. *Advanced Powder Technology* **34**, 104004 (2023).
93. Mayer, J. K. *et al.* Influence of the Carbon Black Dispersing Process on the Microstructure and Performance of Li - Ion Battery Cathodes. *Energy Tech* **8** (2020).
94. Weber, M., Mayer, J. K. & Kwade, A. The Carbon Black Dispersion Index DI CB : A Novel Approach Describing the Dispersion Progress of Carbon Black Containing Battery Slurries. *Energy Tech* **11** (2023).
95. Bockholt, H., Haselrieder, W. & Kwade, A. Intensive powder mixing for dry dispersing of carbon black and its relevance for lithium-ion battery cathodes. *Powder Technology* **297**, 266–274 (2016).
96. Zhang, W. *et al.* Interfacial Processes and Influence of Composite Cathode Microstructure Controlling the Performance of All-Solid-State Lithium Batteries. *ACS applied materials & interfaces* **9**, 17835–17845 (2017).
97. Rosenbach, C. *et al.* Visualizing the Chemical Incompatibility of Halide and Sulfide - Based Electrolytes in Solid - State Batteries. *Advanced Energy Materials*, 2203673 (2022).

Acknowledgements

M.K., F.F., J.J. and A.K. acknowledge financial support by Deutsche Forschungsgemeinschaft (DFG, German Research Foundation) through the priority program 2289 (project 462470125) and by BMBF through the projects 03XP0430A, 03XP0430C (FestBatt Cluster of Competence, FB2-Thio) and 03XP0590D (FoFeBat).

Language and grammar of the manuscript have partially been improved with the help of *DeepL Write* and *ChatGPT4.0* (by OpenAI).

Authors Contributions

M.K. and F.F. contributed equally to this work. M.K., F.F., A.K. and J.J. conceived the project. M.K. and F.F. designed and coordinated the experiments. F.F. prepared the mixtures with the help of N.L., measured the porosities, carried out DEM simulations of the mixing process and analyzed the data. M.K. carried out the electrochemical investigations with help of A.L., measured and analyzed the EDX-SEM and XPS data. T.D. carried out the STEM-EDX and TEM investigations.

D.W. analyzed the XRD data. M.K. and F.F. wrote the first version of the manuscript which was edited by all authors.

Conflict of Interest

The authors declare no conflict of interest.

Table 1 | Overview about samples for the different investigations presented in this study.

Fig. 1 | Concept of the mixed conducting matrix coating approach. **a** Starting materials with different particle size distributions are **b** mixed in a high-intensity mixer with varying rotational speed n , mixing times t_{mix} , compositions, and constant filling degree φ leading to mechanofusion. **c** NCM host particles are coated with an electron and ion conducting matrix, forming building blocks that build up an ordered composite cathode microstructure (**d**).

Fig. 2 | Microstructure, PSD and porosity depending on the coating amount. **a** SEM images and EDX maps of four mixtures with decreasing coating amounts. **b** Corresponding PSDs calculated from SEM images segmentation. **c** Porosity of composite pellets measured at 3.45 MPa. Error bars represent the standard deviation of $n = 3$ porosity measurements.

Fig. 3 | TEM images and STEM-EDX maps of coated particles. **a** & **b** Matrix coating building block with composition 80:20:1. **c** & **d** Thin coating with composition of 99:1:0.

Fig. 4 | Coverage types and coverage dependence on coating content. **a** Schematic illustration of different particle types for which a high and low coverage γ can be calculated. **b**, XPS-derived coverage values for samples mixed at 10,000 rpm for 60 minutes, plotted against the weight percentage of coating. Data is shown for composites with and without CB.

Fig. 5 | Effect of mixing intensity on particle morphology, surface coverage, and porosity for a building block composition of 80:20:3. **a** Coverage γ as a function of specific energy input. **b** Porosity of composite pellets under 3.45 MPa prepared from mixtures after 60 minutes, plotted against specific energy input. Error bars represent the standard deviation of $n = 3$ measurements. **c** SEM images and EDX maps of powders mixed at 1,000, 5,000, and 10,000 rpm for 60 minutes as well as the obtained mean circularity of the different building blocks.

Fig. 6 | DEM simulation of the high-intensity mixing and correlation with experimental coverage. **a** DEM simulation snapshot and schematic image of the high-intensity mixer indicating the mixing action. **b** Measured and simulated net specific power depending on process time for different rotational speeds and a composition of 80:20:3. Error bars represent the standard deviation of the net power, calculated over 60 min for the experiment and over 0.5 s for the DEM simulations. **c** Calculated Coverage as function of simulated stress intensity \overline{SI}_{CG} . **d** Calculated coverage as function of simulated stress number \overline{SN}_p . Regions 1 and 2 correspond to low and high \overline{SI}_{CG} , respectively.

Fig. 7 | Structural damage probed with SPED-TEM. **a** TEM brightfield image of coated NCM (80:20:3) with the red box indicating the area of the SPED scan. **b** SPED phase map showing only the pristine layered phase and the coating layer. Black points represent mostly amorphous regions or voids.

Fig. 8 | Carbon black-dependent electronic and ionic transport properties and size-dependent percolation behavior in composite materials. **a** Effective partial electronic and ionic conductivities of the matrix and composite as a function of CB content. **b** Schematic showing the impact of sample dimensions on measurable percolation behavior.

Fig. 9 | Electrochemical performance of half-cells depending on the cathode composite composition ($1C \approx 200 \text{ mA/g} \approx 3 \text{ mA/cm}^2$). **a** Cycling performance when cycled in CCCV mode at 25°C under 80 MPa stack pressure. Error bars represent the standard deviation of at least $n = 2$ cells. **b** Comparison of active specific capacity and CAM utilization. Error bars represent the standard deviation of at least $n = 2$ cells. **c** Differential capacity plots at $0.3C$ and $1C$. **d** Evolution of CAM utilization during cycling. **e** Elastic and plastic portions of force–indentation curves obtained from nanoindentation on CB-LIC pellets, which were prepared by compacting the premix at 380 MPa. Error bars represent the standard deviation of $n = 24$ indentations. **f** Schematic illustration of how mechanical properties of the coating influence microstructure evolution. Elastic coatings enable elastic recovery, preserving interfacial contact, whereas plastic coatings lead to contact loss due to irreversible deformation.

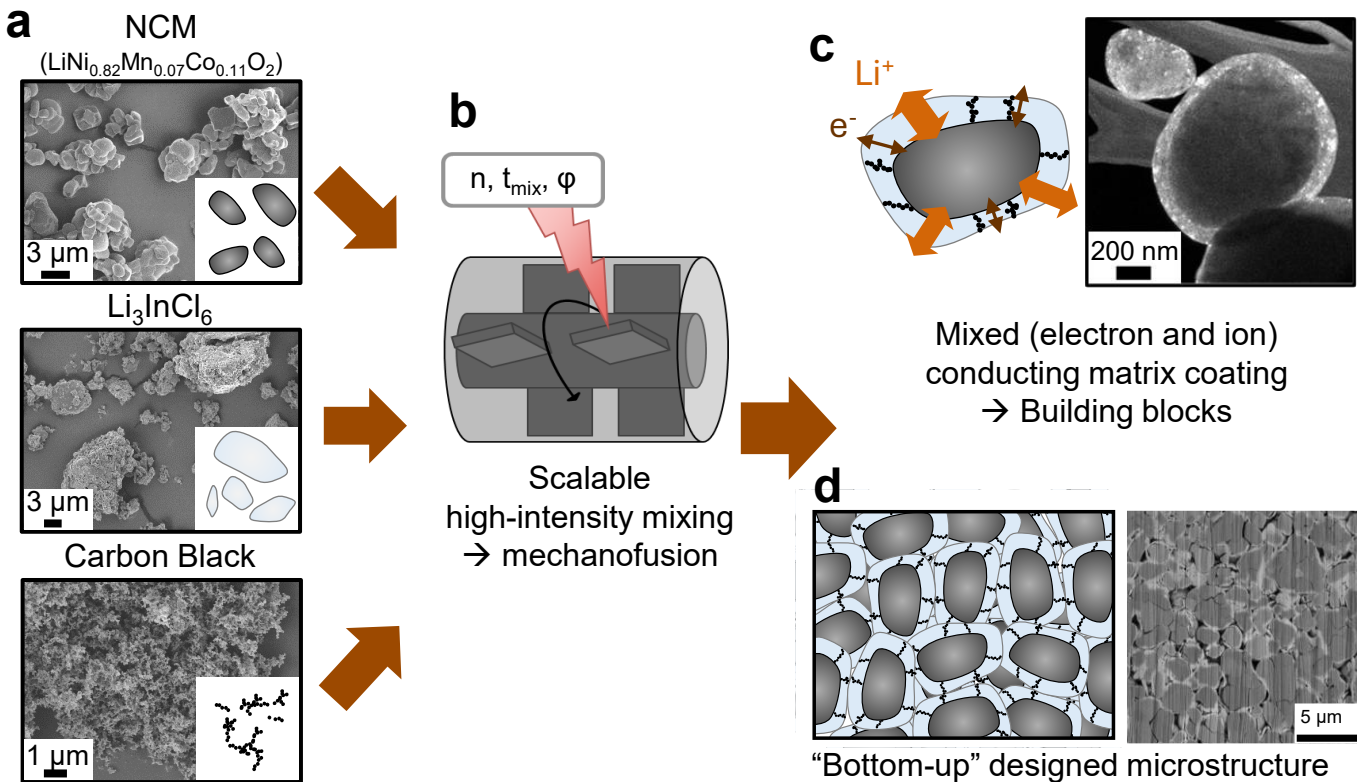
Type of Investigation	Investigated Parameters	Constant Parameters	Nominal Compositions (NCM:LIC:CB, w/w/w)
Coating Thickness Variation (without CB)	Coating Content Variation: 1-20 wt%	-Mixing NCM + LIC: 60 min at 10,000 rpm -Filling degree: 10 %	99:1:0 98:2:0 95:5:0 90:10:0 80:20:0
Coating Thickness Variation (with CB)	Coating Content Variation: 1-20 wt%	-Fixed CB-LIC ratio (20 vol%) -Premixing CB + LIC: 10 min at 5,000 rpm -Mixing Premix + NCM: 60 min at 10,000 rpm -Filling degree: 10 %	99:1:0.2 98:2:0.3 95:5:0.8 90:10:1.5 80:20:3

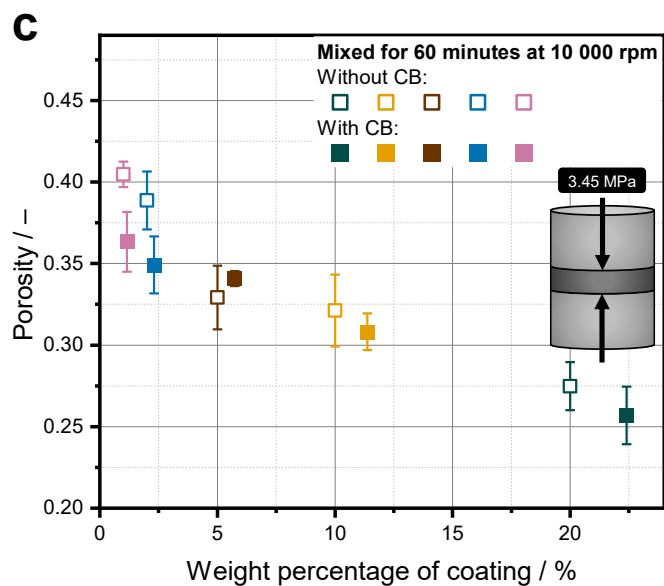
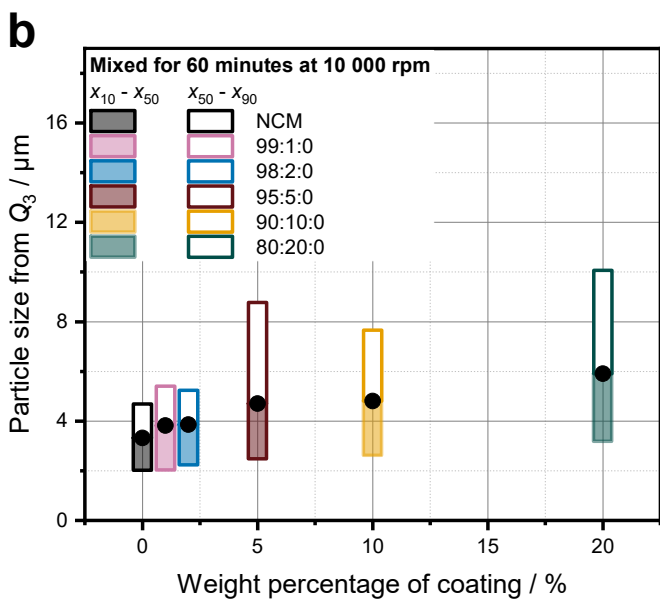
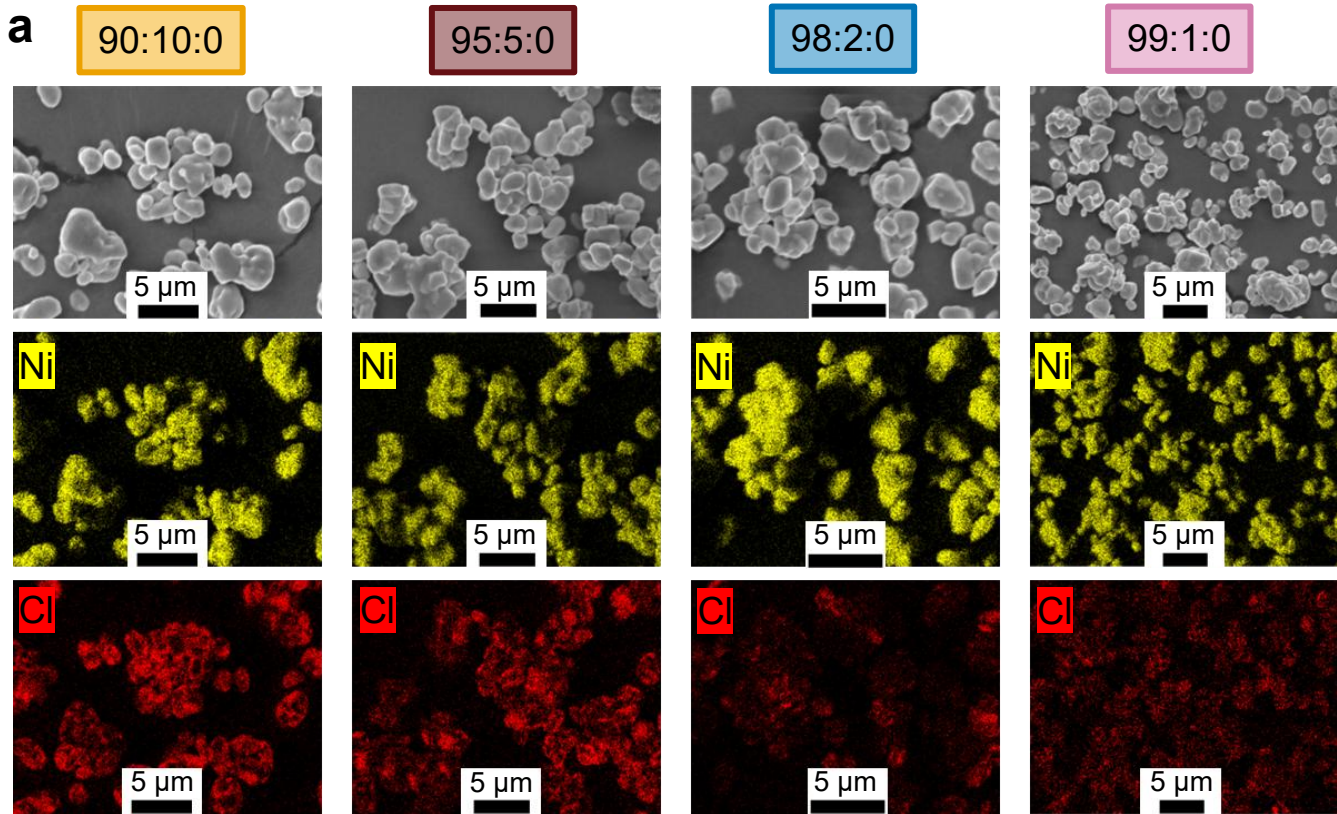
Process Parameter Variation	-Mixing Times: 5, 10, 30 60 min -Rotational speeds: 1,000, 2,500, 5,000, 7,500, 10,000 rpm	-Premixing CB + LIC: 10 min at 5,000 rpm -Filling degree: 10 %	95:5:0.8 80:20:3
Matrix Optimization	CB content variation: 0-3 wt%	-Premixing CB + LIC: 10 min at 5,000 rpm -Mixing Premix + NCM: 60 min at 10,000 rpm -Filling degree: 10 %	80:20:0 80:20:0.2 80:20:0.5 80:20:1 80:20:2 80:20:3

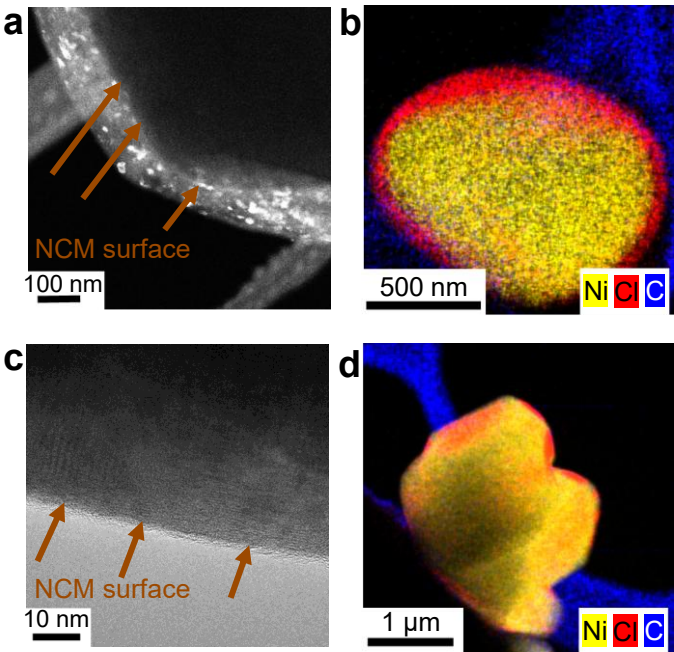
Editor's Summary

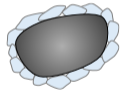
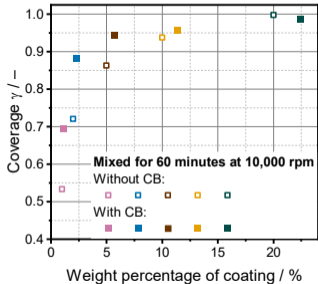
Particle processing plays a critical role in advancing solid state batteries. Here, authors show how solvent-free mechanofusion enables mixed conducting matrix coatings on cathode particles and relate coating quality to macroscopic mixing stresses for scalable solid state battery manufacturing.

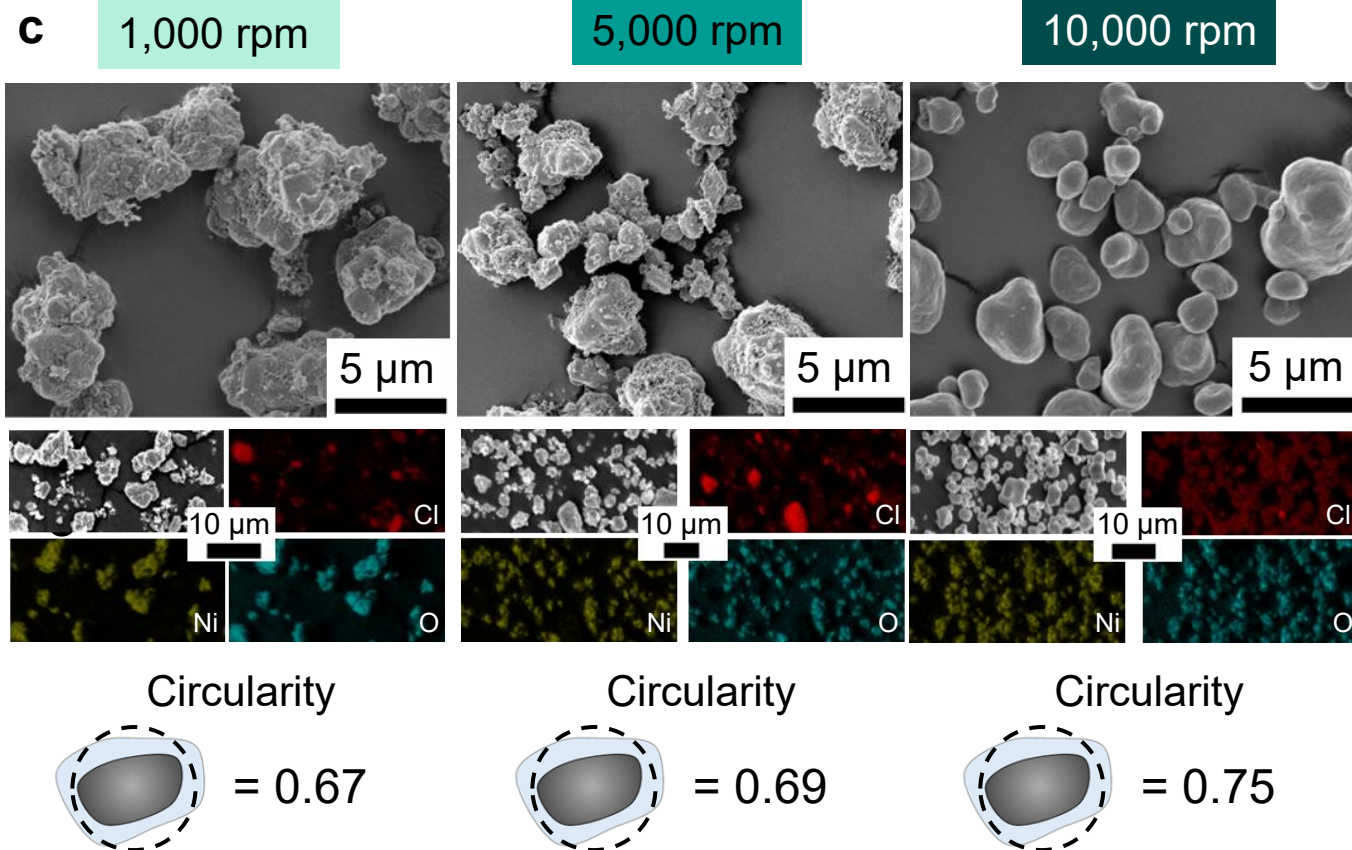
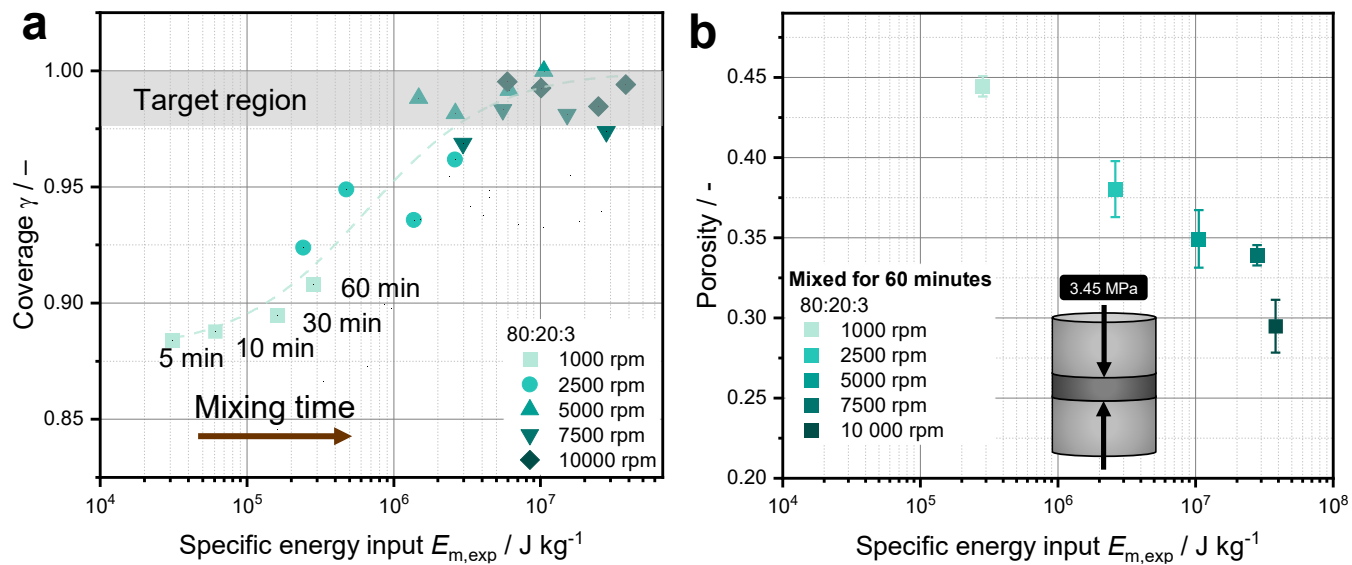
Peer Review Information: *Nature Communications* thanks Bohua Wen and the other, anonymous, reviewer(s) for their contribution to the peer review of this work. A peer review file is available.

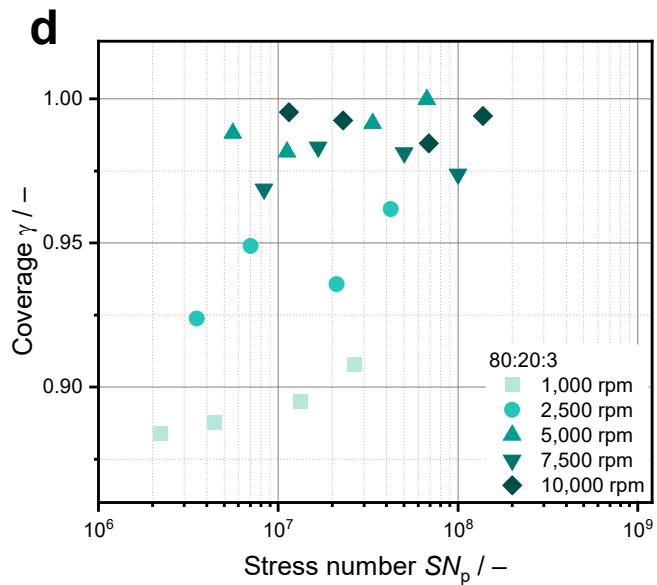
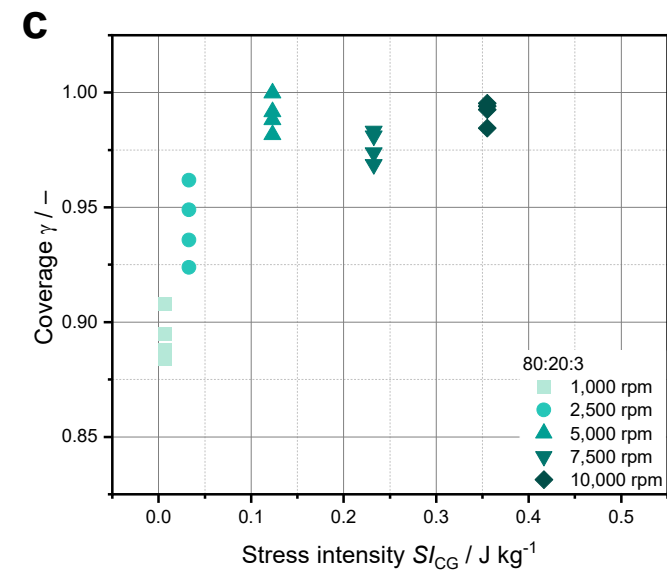
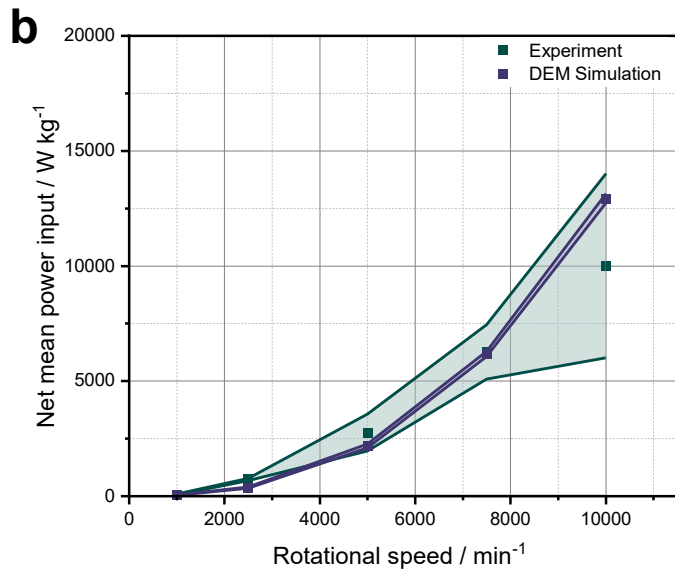
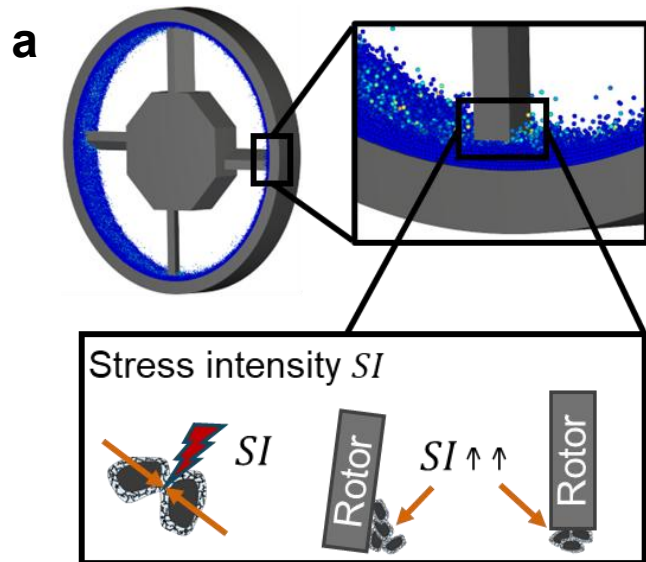


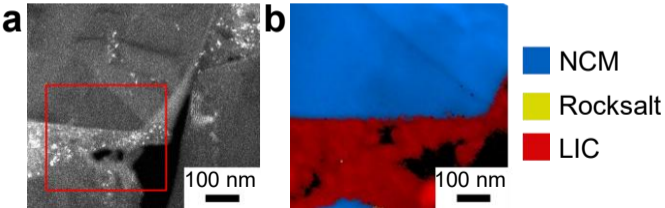




a**High coverage ($\gamma \approx 1$)****Low coverage ($\gamma < 1$)**Covering, thick
(> 10 nm) coatingCovering, thin
(< 10 nm) coatingThick coating with
different morphologyNot fully covering
coating**b**

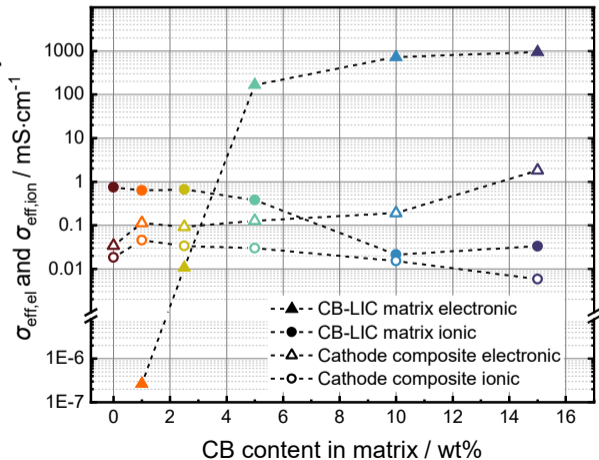






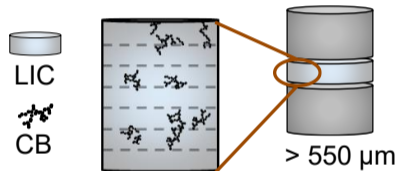
a

Effective Partial Conductivity

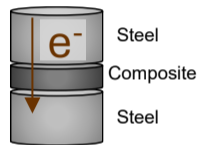
**b**

Measurement of CB-LIC matrix

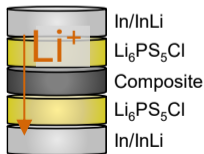
→ Bulk properties:

Non-percolating

Electronic:



Ionic:

 **p_c (finite size) < p_c (bulk) !**

CB-LIC matrix as coating

→ Finite size:

Percolating

